NUMERICAL INVESTIGATION OF THERMAL HYDRAULIC BEHAVIOR OF SUPERCRITICAL CARBON DIOXIDE IN COMPACT HEAT EXCHANGERS

A Thesis

by

ROMA FATIMA

Submitted to the Office of Graduate Studies of
Texas A&M University
in partial fulfillment of the requirements for the degree of

MASTER OF SCIENCE

December 2010

Major Subject: Mechanical Engineering

NUMERICAL INVESTIGATION OF THERMAL HYDRAULIC BEHAVIOR OF SUPERCRITICAL CARBON DIOXIDE IN COMPACT HEAT EXCHANGERS

A Thesis

by

ROMA FATIMA

Submitted to the Office of Graduate Studies of
Texas A&M University
in partial fulfillment of the requirements for the degree of

MASTER OF SCIENCE

Approved by:

Chair of Committee,	Devesh Ranjan
Committee Members,	Kalyana Nakshatrala
	Yassin A.Hassan
Head of Department,	Dennis O'Neal

December 2010

Major Subject: Mechanical Engineering

ABSTRACT

Numerical Investigation of Thermal Hydraulic Behavior of Supercritical Carbon Dioxide in Compact Heat Exchangers. (December 2010)

Roma Fatima, B.E., Birla Institute of Technology and Sciences, India

Chair of Advisory Committee: Dr. Devesh Ranjan

The present work seeks to investigate the thermal hydraulic (heat transfer and fluid dynamics) behavior of supercritical (Sc) fluids at both the fundamental and applied levels. The thermal hydraulics of these fluids is not very well known although they have been used in various applications. There are drastic changes in the thermal and hydraulic properties of fluids at supercritical conditions. There has been a lot of focus to effectively utilize these properties changes in many applications such as heat exchangers.

This work focuses on studying the forced convective heat transfer of Sc-CO_2 in a series of mini semi-circular horizontal tubes and a zig-zag shaped horizontal channel. The problems were investigated numerically by second-order finite volume method using a commercial software FLUENT. Three dimensional Computational Fluid Dynamics (CFD) models were developed to simulate the flow and heat transfer for three different geometries – a single semi-circular channel, a series of nine parallel semi-circular channels and a zig-zag channel. Grid and accuracy refinement studies were carried out to assess numerical errors. All the computational meshes developed for this

study incorporated the first node cell within the viscous sub-layer i.e. $y^+<1$. Since the flow is turbulent, an appropriate choice of turbulence model is highly desirable. Henceforth, various turbulence models were used to study their impact on the heat transfer solution for these problems.

The present numerical work focuses on improving the CFD model and methodologies in order to capture the experimental data of the heat transfer spike at the super critical conditions. Local and average heat transfer coefficients near the critical point were determined from measured wall temperatures and calculated local bulk temperatures. The numerical results are compared with the experiments. The numerical predictions do not convincingly agree with the experiments. This could be because of the incapability of turbulent models to capture the flow physics accurately due to the rapid changes in the fluid properties near critical conditions.

DEDICATION

This thesis is dedicated to my
Grandpa
Grandma
Mom
Baba
Abrar

ACKNOWLEDGEMENTS

I would like to thank my advisor, Dr. Devesh Ranjan, for his constant inspiration, guidance and personal attention while carrying out my master's work. He helped me in making my work a success and gave me the opportunity to learn. I am indebted to him for extending all the necessary support during the course of the work, despite all the work he had. I would also like to give appreciative thanks to my committee members, Dr. Kalyana Nakshatrala and Dr. Hassan Yassin, for their valuable suggestions.

I would like to thank Dr. Mark Anderson who helped improve my technical knowledge on this topic during my visit to the University of Wisconsin at Madison. I am extremely grateful to him for having taught me the right way of approaching problems.

I would also like to thank my group members, Alan Kurizenga and Hongzhi Li, at the University of Wisconsin at Madison for lending their time when needed.

I would also like to thank my friends Sarat, Shankar, Saurabh, Sharmilee, Asmaa, Jacob, Bhanesh, Hoda for their help and support.

Finally, I would like to thank my parents, sister Anam and Asna and my brothers Junaid and Zeeshan for their love, support and continuous encouragement. A special thanks to Abrar for listening to my non-stop discussions.

NOMENCLATURE

Sc	Supercritical
T_{cr}	Critical temperature
V_{cr}	Critical volume
T_{pc}	Pseudo-critical temperature
P_{pc}	Pseudo-critical pressure
P_{cr}	Critical pressure
P_{op}	Operating pressure
T_w	Wall temperature
T_b	Bulk temperature
T_{in}	Inlet temperature
Nu	Nusselt number
Re_b	Reynolds number evaluated at bulk properties
Pr_b	Prandtl number evaluate at the bulk temperature
Pr_{min}	Prandtl number evaluated either evaluated at bulk or wall temperature (whichever is minimum)
μ_b	Molecular viscosity at bulk temperature
μ_w	Molecular viscosity at wall temperature
k_b	Thermal conductivity evaluated at bulk temperature
k_w	Thermal conductivity evaluated at the wall temperature
C_b	Specific heat capacity evaluated at the bulk temperature
ρ_b	Bulk density

ρ_w	Wall density
i_b	Bulk enthalpy
$\dot{m}$	Mass flow rate
M	Mass flux
r	Grid refinement factor
e_a	Relative error
e_{ext}	Extrapolated relative error
GCI	Grid Convergence Index
HTC	Heat Transfer Coefficient
q	Heat flux

TABLE OF CONTENTS

Page

CHAPTER Page

LIST OF FIGURES

Page

Page

Page

Page

Page

LIST OF TABLES

Page

CHAPTER I

INTRODUCTION

Reducing the cost of electricity has been a goal for the power plant industry. This can be achieved by increasing the efficiency of the existing thermodynamic cycles or by reducing the size of the components used in these cycles. One of the ways to achieve a reduction in the size of the cycle is by using compact heat exchangers. This in turn can be achieved by using fluids at supercritical (Sc) conditions having varying thermo-physical properties. The varying thermo-physical properties affect the heat transfer in these fluids. The heat transfer either deteriorates or enhances based on the operating conditions. The enhancement in the heat transfer would be beneficial in these heat exchangers and other applications.

Thus the design and performance of heat exchangers with Sc fluids has been an ongoing research. Water was the fluid to be initially used at supercritical conditions. However, water is very corrosive in nature and henceforth, CO_2 was the next preferred fluid. Some of the reasons for the choice of CO_2 are that it is available in abundance in nature, non toxic, non-flammable with zero ozone depletion potential, which could be one of the most economic and safe natural solutions. Implementing compact heat exchangers with CO_2 at supercritical conditions in Brayton cycles (nuclear power plants) for improving the efficiency of the cycle is one of its primary applications.

This dissertation follows the style and the format of *Experimental and Thermal Fluid Sciences*.

However, this concept is yet to be practically implemented in the industry as there is a need to study the thermal-fluid behavior of supercritical fluids in more detail. Also a comparison of turbine sizes for steam, helium, and Sc-CO_2 performed by Dostal *et al.* has shown that Sc-CO_2 turbines (and compressors) are very compact, requiring a smaller plant footprint [1].

1.1 Characteristics of Sc fluids

Every fluid has a thermodynamic critical point (temperature and pressure) where the distinction between vapor and liquid disappears. Any fluid that operates above this temperature and pressure is called the supercritical fluid. It is characterized by the unique state parameters - critical temperature T_{cr}, critical volume V_{cr} and critical pressure P_{cr} [2]. At the critical point, densities of the equilibrium liquid phase and the saturated vapor phase become equal. The new phase has some properties similar to liquids and some others to vapor. The critical point of carbon dioxide, fluid of interest in the current study, is at a temperature of 30.95°C and a pressure of 7.38MPa

The most significant thermo-physical property variations occur near the critical and the pseudocritical point. (A pseudocritical point, P_{pc} and T_{pc} is the point corresponding to maximum specific heat at a given pseudocritical pressure ($P_{pc}>P_{cr}$) pseudocritical temperature ($T_{pc}>T_{cr}$). [2]

The pseudocritical temperature of CO_2 as a function of pressure can be best fitted by the following algebraic equation [3]:

$$T_{pc} = -122.6 + 6.124p - 0.1657p^2 + 0.0177p^{2.5} - 0.000560p^3 \qquad (1\text{-}1)$$

There are variations in the properties of fluids in the pseudo critical region which can be used as an advantage in the design of heat exchangers. Figure 1.1 shows the variations in properties of CO_2 as it passes through the critical temperature. It is observed that there is a discontinuity in the properties at critical conditions.

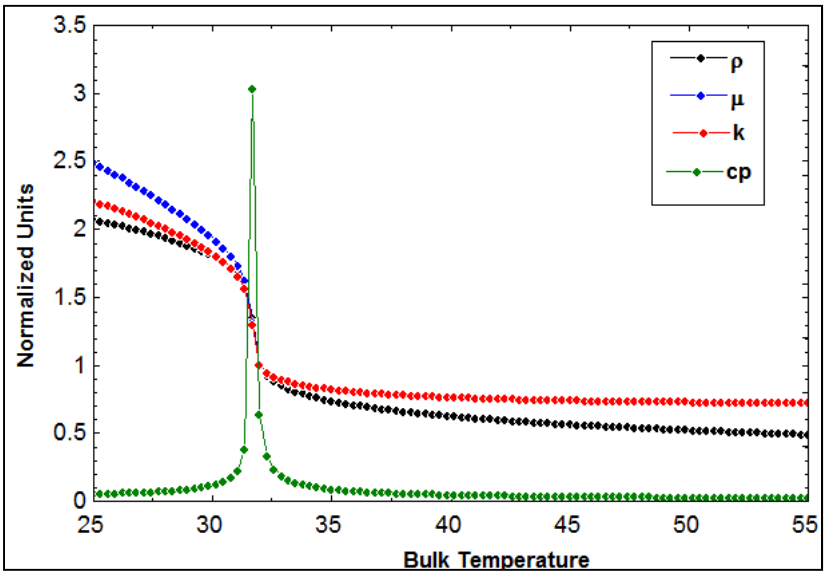

Figure 1.1: Normalized thermophysical properties of supercritical CO_2

Figure 1.2 shows the variation of specific heat at various fluid temperatures and pressures for carbon dioxide. It can be noted that the specific heat peaks at the critical temperature. It can also be observed that the specific heat is the maximum at the critical pressure (7.38MPa). As the pressure increases beyond the critical pressure, the peak in specific heat reduces and shifts towards higher temperatures. Moreover, this peak also broadens away from the critical pressure. As the pressure goes below or way above the

critical pressure the fluid behaves like an ideal gas. The heat transfer enhances because of this increase in the specific heat. This property is favorable for power cycles in the heat exchanger region where high heat transfer is desirable.

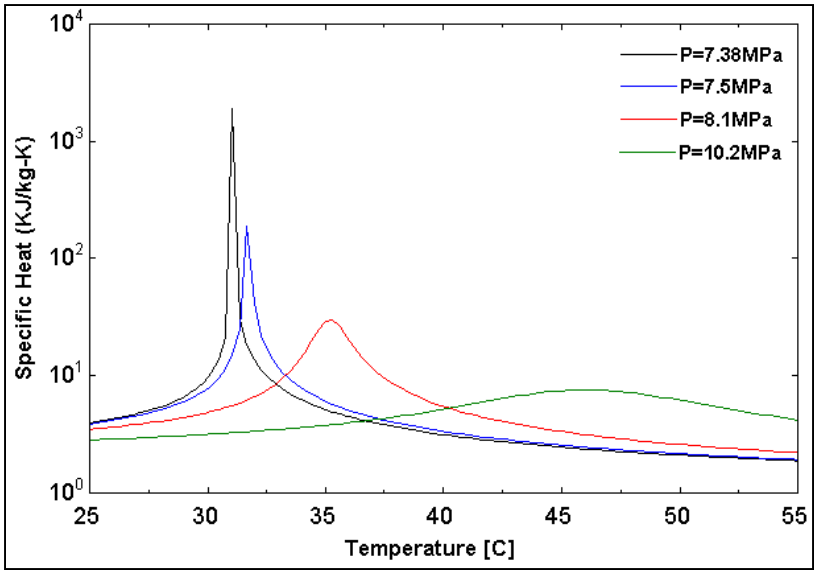

Figure 1.2: Specific heat capacity of super-critical CO_2 at different pressures

The density variation at the critical and pseudocritical points is shown in Figure 1.3 at different temperatures and pressures. It is observed that there is a drastic decrease in the density of CO_2 at the critical and pseudocritical points. Operating the pre-cooler at pseudocritical temperatures and pressures helps in reducing the compressor work ($W_{comp} = \rho V \Delta h$) when used in power cycles and thereby increasing the overall plant

efficiency. A detailed discussion of the use of supercritical fluids and the advantages associated is provided in the next section.

The variation of thermal conductivity and molecular viscosity with bulk temperature for different pressures is shown in Figures 1.4 and 1.5. It is observed that both the thermal conductivity and the molecular viscosity drop at the critical temperature. As the pressure moves away from the critical pressure this decrease in the properties reduces.

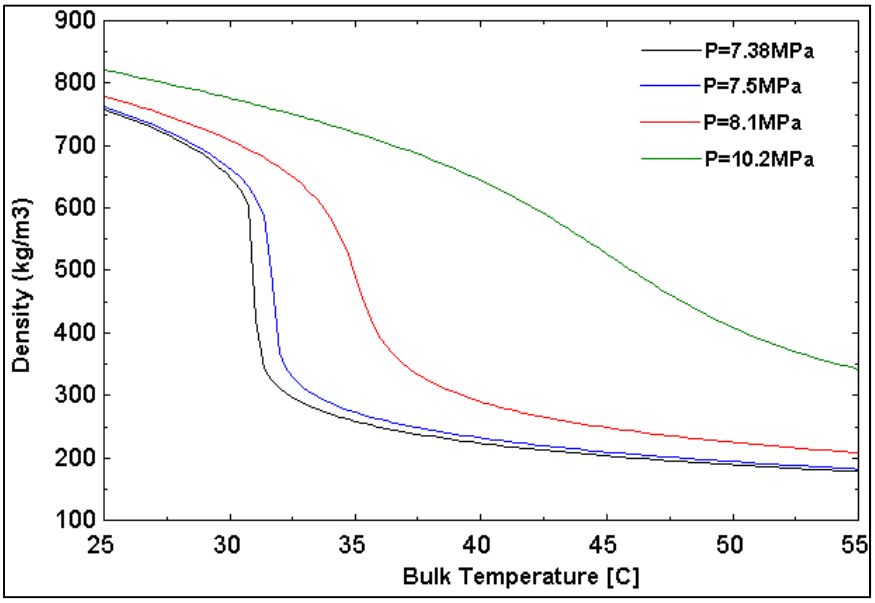

Figure 1.3: Variation of density with temperature at critical and pseudo critical pressure of CO_2

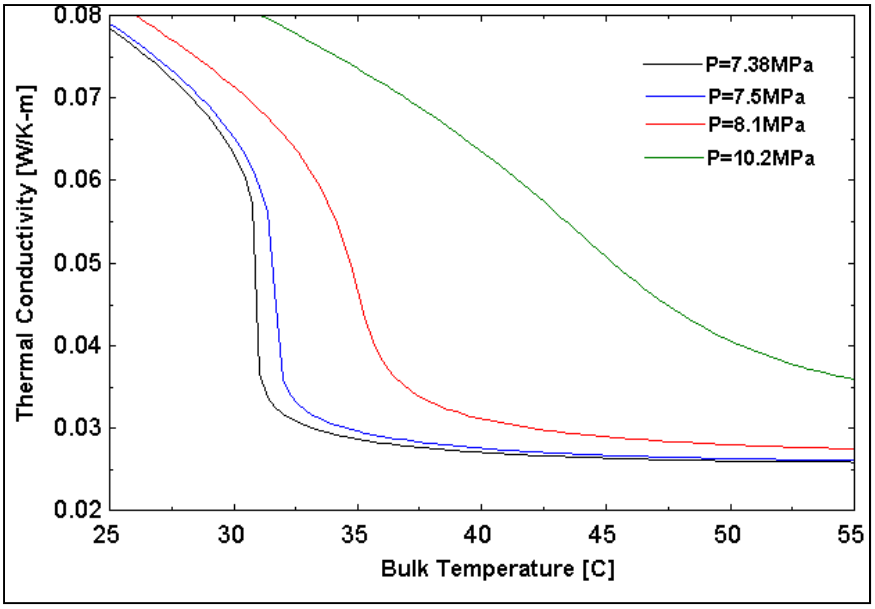

Figure 1.4: Variation of thermal conductivity with temperature at critical and pseudo critical pressure of CO_2

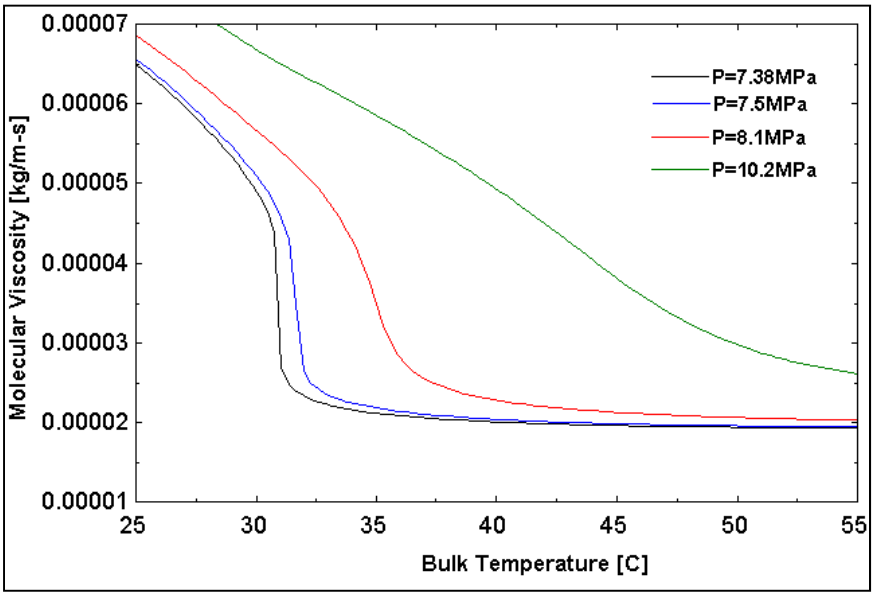

Figure 1.5: Variation of molecular viscosity with temperature at critical and pseudo critical pressure of CO2

1.2 Motivation and importance

Sc-CO_2 can be used in various thermodynamic cycles such as the Brayton and Rankine cycle to improve the efficiency and reduce capital cost. However, these fluids are not usually used in Rankine cycles because of the phase change in turbine which can cause excessive wear. As compared to a Rankine power conversion cycle, the turbo-machinery required for the Sc-CO_2 Brayton power conversion cycle is more compact and less expensive, and has shorter construction periods [4].

Figure 1.6 shows the layout of a simplest version of the Brayton cycle. Brayton cycles uses fluid in gas phase for power generation. Brayton cycle consists of the compressor, turbine, reactor and the heat exchanger. The pre-cooler and the recuperator are the heat exchangers used in the cycle. The pre-cooler cools the fluid to the desired temperature before it enters the compressor. The recuperator sometimes called regenerator (makes use of the waste heat from the compressor which would otherwise be rejected into the atmosphere) consists of the working fluid on both the sides flowing at different mass flow rates operating at different temperatures. This is used to preheat the fluid before it enters the reactor. The conventional Brayton cycles usually uses low density fluid which causes a large amount of power generated by the turbine to be consumed by compressors making the cycle less efficient. The compressor work could be reduced by operating the cycle at Sc pressures and temperatures. The problem of phase change does not occur since it operates above the vapor dome.

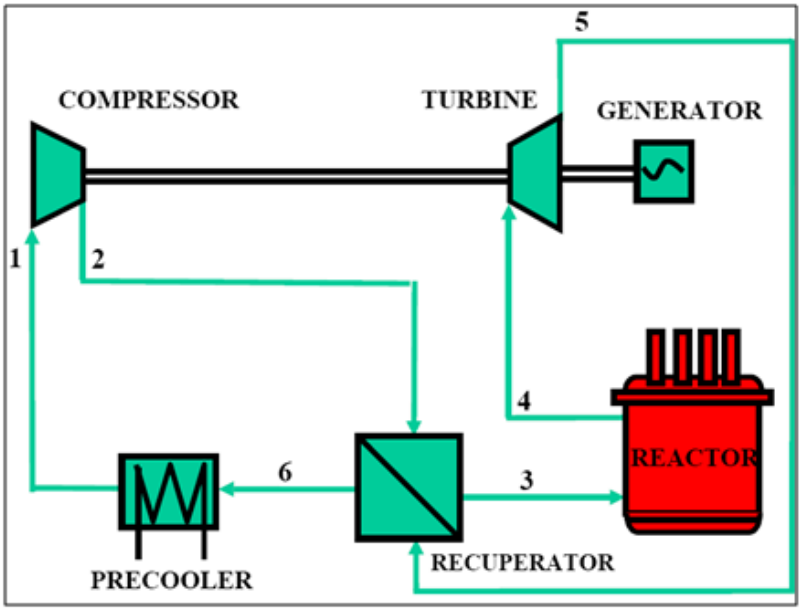

Figure 1.6: Simple Brayton cycle [1]

The various state points are indicated on the T-s diagram as shown in Figure 1.7 State points 1, 2 and 6 operate close to the critical pressure. State points 3, 4 and 5 operate at Sc pressure. It is desired that state point 1 operates close to the critical point to reduce the compressor work because of the drop in density at pseudocritical conditions. The exit temperature of the pre-cooler is closely related to the overall efficiency of the cycle. Figure 1.8 shows the variation of cycle efficiency with respect to the outlet temperature of the pre-cooler. It can be observed that the cycle efficiency is the maximum at a temperature of 30.95°C (i.e. critical temperature of CO_2). It is difficult to maintain the outlet temperature at 30.95°C during the entire duration of the cycle. A slight drop in this temperature would make the fluid sub-critical causing two-phase flow

in the compressor which leads to cavitations in compressors thereby reducing its life. The pressure is maintained slightly above the critical pressure 7.38MPa so that a slight fluctuation in the system does not drop the operating pressure below its critical value.

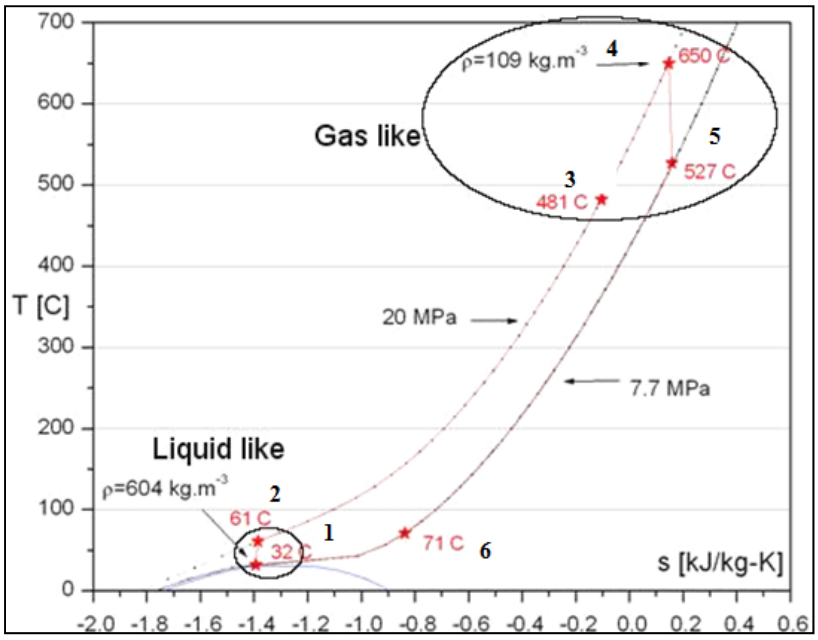

Figure 1.7: T-s plot of the operating states in a Brayton cycle [1]

The work done by the turbine does not depend on the operating pressure. Rather it depends on the pressure ratio. The fluid in the turbine behaves like an ideal gas. It is only at very high pressures this ideal behavior deviates. However, at very high pressures the turbine material may have structural limitations like creep strain, fatigue, etc which restricts its operation at such pressures. The compressor operates at the critical point, and there is a significant deviation of fluid from ideal behavior. Both the pressure ratio as

well as the operating pressure affects the compressor work when it is operated at critical temperature. The compressor work drops at critical conditions because of the density drop. The rise in pressure in the compressor is lesser compared to the turbine [1].

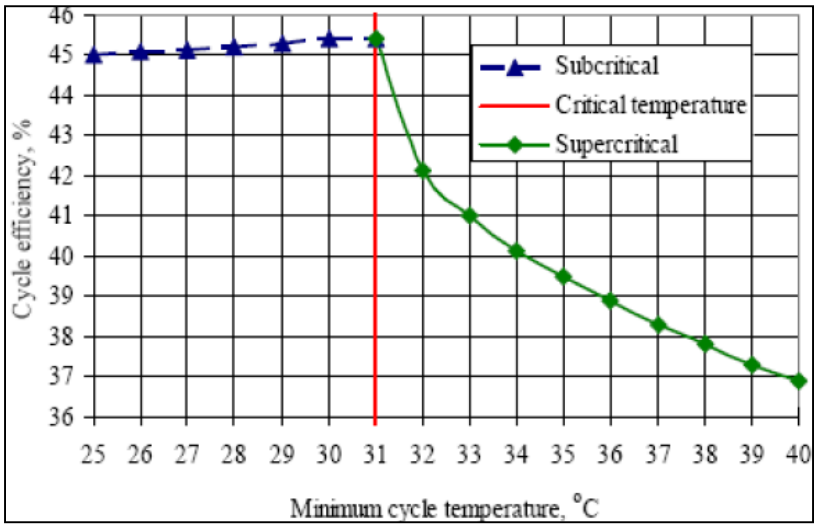

Figure 1.8: Cycle efficiency variation with outlet temperature of the pre-cooler [1]

At the critical point there is also an increase in the specific heat capacity which affects the design of a recuperator and pre-coolers (heat exchanger). Use of Sc fluids in heat exchangers especially in the Printed Circuit Heat Exchanger (PCHE) which are compact has been the focus of researchers.

The PCHE was first made in Australia. It was later implemented in refrigerator technology by the company Heatric which became a forerunner in recuperator designs due to its compact form, high heat transfer capability, and ability to withstand high pressures. Recent investigations concerning heat transfer characterization of a

commercially available PCHE using CO_2 as the hot and cold working fluid has been published [5]. However these heat exchangers were tested at operating pressures and temperatures away from pseudocritical temperatures, where negligibly small thermo physical changes occur, with the lowest temperature being 90^{o}C.

A significant amount of research has been carried out in the vicinity of critical point for various operating conditions to understand the heat transfer characteristics for these heat exchangers.

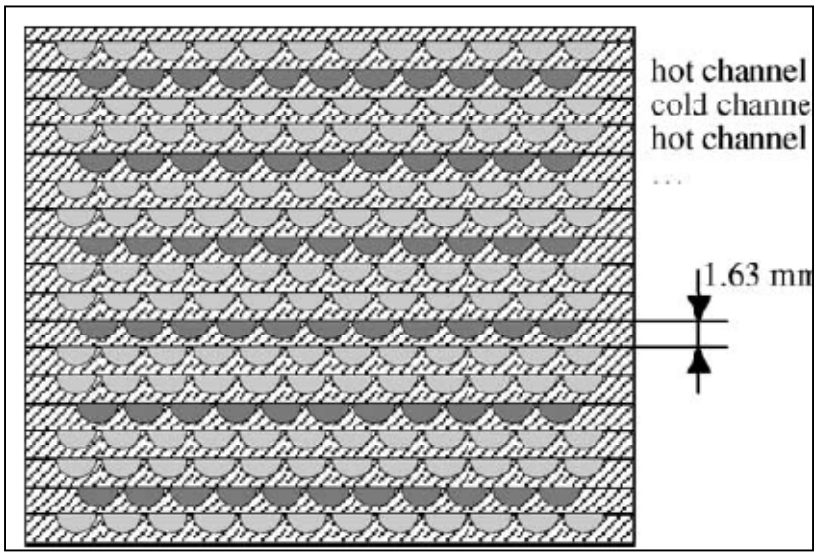

Figure 1.9: Printed Circuit Heat Exchangers (PCHE) [4]

The PCHE normally consists of two zigzag type flow channels, one for the hot fluid and one for the cold fluid, etched into stainless steel plates. The plates are then diffusion bonded (solid state joining of metals and ceramics capable of joining both

small and large components). A similar design is used in this study but instead of having zigzag channels, semi-circular channels are etched into 316 stainless steel plates. These channels are 1.9 mm in diameter and 500 mm in length. The experimental work has been carried out at University of Wisconsin at Madison to investigate the conditions for heat transfer enhancement and deterioration through these channels. Due to cost constraints, recent advances in engineering have been made by performing numerical calculations than conducting experiments. The main contribution of this thesis is to perform a numerical study of Sc-CO2 in a semi-circular and a zigzag channel. The numerical investigation is carried out using the commercial CFD code FLUENT 12.0 which solves the Navier-Stokes equations numerically [5]. An in-depth analysis of this problem is performed and documented in this thesis.

1.3 Organization

The previous chapter gives a brief introduction of the problem that is of interest in this research. Chapter II provides the background information and literature survey. Chapter III gives brief information of the experimental facility at University of Wisconsin-Madison. Chapter IV introduces to the numerical modeling procedure. Chapter V gives details of the geometry, the mesh studies and the boundary conditions used for the problem. Chapter VI discusses the comparison of heat transfer in single and nine channel geometry and compares it to experiments. The effect of pressure and the mass flux on the heat transfer is also provided in this section. It also discusses the difference in the heat transfer observed in the heating and cooling mode conditions. It also offers some of the preliminary numerical work done in zig-zag channels.

CHAPTER II

LITERATURE SURVEY

2.1 Background

Research on the heat transfer of Sc-fluids dates back to the 1930s with the work done by Schmidt *et al.* to study the heat transfer of super-critical fluids [6]. His work focused on investigating the heat transfer of fluids near-critical point in order to develop a new effective cooling system for turbine blades in jet engines. It was found that heat transfer increased near the critical point and this advantage was used in single-phase thermosyphons [7]. Since then researchers are focusing on making use of the drastic property changes that occur near the critical point in various applications. The idea of using Sc water gained momentum in 1950s for its use in steam generators to increase the efficiency of fossil-fired power plants [8]. Extensive work was done between 1950s and 1980s; several concepts of nuclear reactors cooled with water at supercritical pressures were developed. This idea was abandoned for 30 years and recently researchers realized that fluids at Sc conditions could be used to improve the efficiency and performance of nuclear power plants. But instead of water the research now focused on CO_2 because of the reasons stated in Chapter I. The use of Sc- CO_2 is expected to implement in the Generation IV power plants by 2015-2020. This would significantly improve the efficiency up to 40-45%, decrease the reactor coolant pumping power, reduce the frictional losses and eliminate dry-outs [2]. Therefore the need for studying the thermal and hydraulic of these fluids is vital.

2.2 Heat transfer correlations

Extensive work has been carried out in order to develop empirical correlations for predicting the heat transfer coefficients based on the limited experimental data. Due to the complicated nature of the fluid flow in miniature channels there is no valid theoretical heat transfer correlation. This leads to various empirical correlations which tend to use a range of experimental condition in different geometries. Many investigations of the heat transfer phenomenon with water and CO_2 have been implemented; however the correlations discussed below are widely used to compare experimental data. Of the available Nusselt correlations the Jacksons and Krasnoschekov correlations have been found to capture the heat transfer in tubes in the absence of buoyancy effects. The Liao's correlation takes the effect of buoyancy on the heat transfer and is found to be accurate [3].

The first empirical correlation for Nusselt number which was thought to be used by McAdams (1942) for heat transfer in turbulent flows at sub-critical pressures was the Dittus-Boelter correlation.

$$Nu = 0.0243 Re_b^{0.8} Pr_b^{0.4} \qquad (2\text{-}1)$$

where Nu is the Nusselt number, and Re_b and Pr_b are respectively, the Reynolds and the Prandtl number evaluated at the bulk fluid properties. This correlation was found to be in good agreement for fluid flow in circular tubes at low heat fluxes and high pressures (31MPa) for any fluid, but did not predict reasonable results at pressures close to critical pressure because it did not consider the variation in properties close to critical pressures. This correlation was used as a base for modified heat transfer correlations [9].

Shitsman in 1959 analyzed the experimental data for heat transfer in Sc-water flowing inside tubes; he generalized this data with Dittus-Boelter type correlation and proposed a new empirical correlation for evaluating the heat transfer coefficient [10]:

$$Nu = 0.023 Re_b^{0.8} Pr_{min}^{0.4} \tag{2-2}$$

where "*min*" means minimum Prandtl number either evaluated at the bulk fluid temperature or evaluated at the wall temperature whichever is smaller. Shitsman based the above correlation by assuming that the thermal conductivity is a smoothly decreasing function of the temperature near the critical and the pseudo critical points. But thermal conductivity varies when the operating conditions are close to critical conditions. Thus there was a need for further investigation [10].

Swenson *et al.* in 1965 studied heat transfer to Sc water in smooth-bore tubes. Their results showed that the conventional correlations did not work well because of rapid changes in thermo physical properties of supercritical water in the pseudo critical region [11].

Krasnoshchekov and Protopopov in 1967 proposed an empirical correlation for forced convective heat transfer in water and carbon-dioxide at supercritical pressures in circular tubes. The Prandtl number and the specific heat were averaged over the ranges to account for the thermo-physical property variations [12]:

$$Nu = Nu_0 \left(\frac{\mu_b}{\mu_w}\right)^{0.11} \left(\frac{k_b}{k_w}\right)^{-0.33} \left(\frac{\bar{c}_p}{c_{pb}}\right)^{0.35} \tag{2-3}$$

$$Nu_0 = \frac{\frac{\varepsilon}{8} Re_b \overline{Pr}}{12.7\sqrt{\frac{\varepsilon}{8}}\left(\overline{Pr}^{2/3}-1\right)+1.07} \tag{2-4}$$

$$\varepsilon = \frac{1}{(1.82log_{10}Re_b - 1.64)^2} \tag{2-5}$$

The above equation was modified in 1971 in order to take the effect of tube entrance region [13]:

$$Nu = Nu_0 \left(\frac{\rho_w}{\rho_b}\right)^{0.3} \left(\frac{\bar{c}_p}{c_{pb}}\right)^n \left(0.95 + 0.95\left(\frac{x}{D}\right)^{0.8}\right) \tag{2-6}$$

where

$$\text{n=0.4 at } \frac{T_w}{T_{pc}} < 1 \text{ or } \frac{T_b}{T_{pc}} > \geq 1.2 \tag{2-7}$$

$$\text{n=} n_1 = 0.22 + 0.18\frac{T_w}{T_{pc}} \text{ at } 1 \leq \frac{T_w}{T_{pc}} \leq 2.5 \tag{2-8}$$

$$\text{n=} n_1 + (5n_1 - 2)\left(1 - (\frac{T_b}{T_{pc}})\right) \text{ at } 1 \leq \frac{T_b}{T_{pc}} \leq 1.2 \tag{2-9}$$

where $\bar{c}_p = \frac{i_b - i_w}{T_b - T_w}$, ρ_w is the density evaluated at the wall temperature, ρ_b is the density at the bulk fluid temperature.

Yamagata in 1972 investigated forced convective heat transfer to Sc water flowing in tubes [14]. The following empirical correlation was recommended:

$$Nu_b = 0.035 Re_b^{0.85} Pr_b^{0.8} F_c \tag{2-10}$$

where F_c is factor which varies based on the ratio of $\frac{(T_{pc} - T_b)}{(T_w - T_b)}$.

$$F_c = 1 \text{ for } E > 1 \tag{2-11}$$

$$F_c = 0.67 Pr_{pc}^{-0.05} \left(\frac{\bar{c}_p}{c_{pb}}\right)^{n2} \text{ for } 0 \leq E \leq 1, \tag{2-12}$$

$$F_c = \left(\frac{\bar{c}_p}{c_{pb}}\right)^{n2} \text{ for } E > 1 \tag{2-13}$$

$$E = \frac{(T_{pc} - T_b)}{(T_w - T_b)} \tag{2-14}$$

$$n_1 = -0.77\left(1 + \frac{1}{Pr_{pc}}\right) + 1.49 \tag{2-15}$$

$$n_2 = -1.44\left(1 + \frac{1}{Pr_{pc}}\right) - 0.53 \tag{2-16}$$

Here n_1 and n_2 are factors which take the effect of Pr number in the pseudocritical region to predict the heat transfer.

Jackson and Fewster in 1975 modified the above correlation and proposed a new one which was similar to the Bishops correlation (1964) [15] without taking the geometrical parameters into it [16].

$$Nu = 0.0183 Re_b^{0.82} \overline{Pr}^{0.5} \left(\frac{\rho_w}{\rho_b}\right)^{0.3} \tag{2-17}$$

The above correlation was modified in 2002 as it did not take the effect of varying specific heat to predict the heat transfer [17]:

$$Nu = 0.0183 Re_b^{0.82} \overline{Pr}^{0.5} \left(\frac{\rho_w}{\rho_b}\right)^{0.3} \left(\frac{\overline{c_p}}{c_{pb}}\right)^n \tag{2-18}$$

where n varied based on the bulk and wall temperatures as:

$$\text{n=0.4 at } T_b < T_{pc} < T_w \text{ and } 1.2T_{pc} < T_b < T_w \tag{2-19}$$

$$\text{n= } 0.4 + 0.2\left(\frac{T_w}{T_{pc}} - 1\right) \text{ at } T_b < T_{pc} < T_w \tag{2-20}$$

$$\text{n=} n_1 + (5n_1 - 2)\left(1 - (\frac{T_b}{T_{pc}})\right) \text{ at } T_{pc} < T_b < 1.2T_{pc} \text{ and } T_b < T_w \tag{2-21}$$

In 2000 Petterson *et al.,* studied the heat transfer and pressure drop characteristics of evaporating carbon dioxide in flat multiport extruded aluminum micro channel tubes. The tube consists of 25 circular ports with 0.79 mm inner diameter. The

experiments were performed with mass flux 200-600 kg/m^2-s, evaporation temperature 0-20°C and heat flux 5-20 kW/ m^2. The overall heat transfer coefficient was measured with water-to- CO_2 heat transfer, and the CO_2 –side heat transfer coefficient was evaluated using the Wilson plot technique to calibrate an equation for the water-side heat transfer coefficient. The results showed that for certain volume fractions the heat transfer dropped and this effect was more pronounced for high mass fluxes and evaporation temperatures [18].

In 2002, Liao *et al,* studied the effect of convective heat transfer in horizontal and vertical miniature circular tubes of diameters 0.7, 1.4, 2.16 mm using CO_2. The pressure was varied from 7.4 to 12.0MPa, temperature from 20°C to 110°C and mass flow rate from 0.02 to 0.2 kg/min. It was found from his experiments that buoyancy effects were significant for all flow orientations though the Reynolds number of the flow was as high as 10^5. When $\frac{Gr}{Re_b^2} < 10^{-3}$ the buoyancy effects were negligible, this is the theoretical criteria to investigate the effect of buoyancy on the flow in horizontal channels. The accuracy of these criteria was compared to the experimental data obtained in these miniature channels; it was observed that buoyancy effect was less significant for small tubes.

The experimental results also showed that there was impairment of heat transfer in downward flow but the heat transfer for horizontal and upward flow was enhanced. Based on the experimental data, Nusselt number correlations were obtained for all flow orientations. In horizontal flow, the following empirical correlation was obtained for

heat transfer in these tubes heated at an approximate constant temperature based on a least square fit of 68 experimental data.

$$Nu_b = 0.124 Re_b^{0.8} Pr_b^{0.4} \left(\frac{Gr_m}{Re_b^2}\right)^{0.203} \left(\frac{\rho_w}{\rho_b}\right)^{0.842} \left(\frac{\bar{c}_p}{c_{pb}}\right)^{0.384} \quad (2\text{-}22)$$

In upward flow, a least square fit of 66 experimental data for these tubes heated at constant temperature yield the following empirical correlation:

$$Nu_b = 0.354 Re_b^{0.8} Pr_b^{0.4} \left(\frac{Gr_m}{Re_b^{2.7}}\right)^{0.157} \left(\frac{\rho_w}{\rho_b}\right)^{1.297} \left(\frac{\bar{c}_p}{c_{pb}}\right)^{0.296} \quad (2\text{-}23)$$

In downward flow, a least square fir of 70 experimental data points lead to the empirical correlation equation as follows:

$$Nu_b = 0.643 Re_b^{0.8} Pr_b^{0.4} \left(\frac{Gr_m}{Re_b^{2.7}}\right)^{0.186} \left(\frac{\rho_w}{\rho_b}\right)^{2.154} \left(\frac{\bar{c}_p}{c_{pb}}\right)^{0.751} \quad (2\text{-}24)$$

where Gr_m the mean Grasholf number is defined as $Gr_m = \frac{(\rho_w - \rho_b) g d^3}{\rho_b \vartheta_b^2}$, ρ_w is the density evaluated at the wall temperature,$\rho_b$and c_{pb} is the density and the specific heat evaluated at the bulk mean temperature [3].

In 2005 Huai et al., proposed the Nusselt number correlation in horizontal multi-port extruded aluminum test section consisting of 10 circular channels with an inner diameter of 1.31mm. The local and average pressure drop and heat transfer coefficient was measured for pressures ranging from 7.4 to 8.5MPa, inlet fluid temperature of 22 to 53°C and mass flux from 113.7 to 418.6 kg/m^2-s. There was a large discrepancy between the heat transfers coefficients obtained in this study compared to that reported in the literature. Based on the experimental work, a new empirical correlation was developed

for forced convection of supercritical CO_2 in horizontal multi-port mini channels under cooling.

$$Nu = 0.022186Re^{0.8}Pr^{0.3}\left(\frac{\rho_r}{\rho_w}\right)^{-1.4652}\left(\frac{\bar{c}_p}{c_{pw}}\right)^{0.0832} \quad (2\text{-}25)$$

where c_{pw} and ρ_w are estimated based on the wall temperature, $\rho_r$based on the bulk mean temperature and $\bar{c}_p$ is defined as:$\bar{c}_p = \frac{H_r - H_w}{T_r - T_w}$. All other physical properties are estimated based on the bulk mean temperature of CO_2. The discrepancy between the Liao and Huai's empirical correlation and the measured Nusselt numbers might be attributed to the fact that in the Liao's work a single tube was tested whereas in Huai's work is for an array of tubes [19].

There has been a significant experimental work performed at University of Wisconsin-Madison to study the heat transfer in various geometries. In 2007 Jeremy Licht studied the heat transfer in circular and square annular flow channels for Sc-water. The accuracy and the validity of various heat transfer empirical correlations and buoyancy criteria were compared with the heat transfer measurements. These heat transfer measurements were carried out for varying inlet mass velocities, heat fluxes and inlet temperatures at a pressure of 25MPa. It was found that the Jacksons correlation could best predict the test data capturing almost 86% of the data. There was a good agreement with the high mass velocity data, comparing it to the previous investigators. There was a difficulty in applying these correlations for low mass velocity data to a region of deterioration [20].

Work is being done to study the heat transfer in semi-circular and zig-zag channels by Alan Kurizenga to investigate different heat exchanger flow configuration. His work includes the understanding of the heat transfer phenomenon in Sc-CO_2 near the T_{pc} in the heating and cooling modes in semi circular channels. The experimental data is compared to the various Nusselt correlations. The Jacksons emprical correlation indicated a lack of prediction because it did not take the low system pressure which appeared to be directly proportional to the increasing specific heat. A new emprical correlation is proposed based on the Jacksons correlation [4].

$$Nu_{Horizonatl} = Nu_{Jackson}\left(\frac{C_{p,b}}{C_{p,IG\ at\ Tpc}}\right)^{-0.19} \tag{2-26}$$

where $C_{p,IG\ at\ Tpc}$ is the specific heat of CO_2 assuming the ideal gas behavior evaluated at T_{pc} at a given experimental pressure. Table 2.1 below lists down the work that has been carried out in this area.

Table 2.1: Previous research work to study the heat transfer of supercritical fluids

Author	Year	Main Fluid	Subject
Dittus-Boelter	1930	Any fluid	Turbulent flow in Circular tubes.
Shitsman	1959	Water	Heat transfer flowing in tubes, Heat transfer deterioration and oscillation.
Bishop	1962,1965	Water	Heat transfer, Upward flow.
Swenson	1965	Water	Heat transfer smooth-bore tubes, Heat transfer deterioration.
Krasnoshchekov & Protopopov	1967	Water & Carbon dioxide	Forced convection heat transfer in circular tubes.
Yamagata	1972	Water	Heat transfer, Heat transfer deterioration.
Jackson & Fewster	1975	Carbon dioxide	Heat transfer, buoyancy effect.
Petukov	1979	Carbon dioxide	Heat transfer and pressure drop.
Peterson	2000	Carbon dioxide	Heat transfer and pressure drop in flat multi-port aluminum tube.
Liao	2002	Carbon dioxide	Convective heat transfer in horizontal and vertical miniature tubes.
Huai	2005	Carbon dioxide	Heat transfer in horizontal multi-port aluminum test section consisting of 10 circular channels.
Jeremy Licht, Michael Corradini and Mark Anderson	2007	Water	Heat transfer and buoyancy in circular and square annular channels.
Alan Kurizenga, Mark Anderson	2010	Carbon dioxide	Heat transfer is semi-circular and zigzag channels

CHAPTER III

EXPERIMENTAL FACILITY

In order to perform the numerical studies, an understanding of the experiments facility and its capabilities is required. This section describes the experimental facility at the University of Wisconsin Madison.

The experimental facility consists of two loops, one is for CO_2 to recirculate called the CO_2 recirculation loop and the other loop consists of the heat exchanger test section. Figure 3.1 shows schematic of the experimental facility.

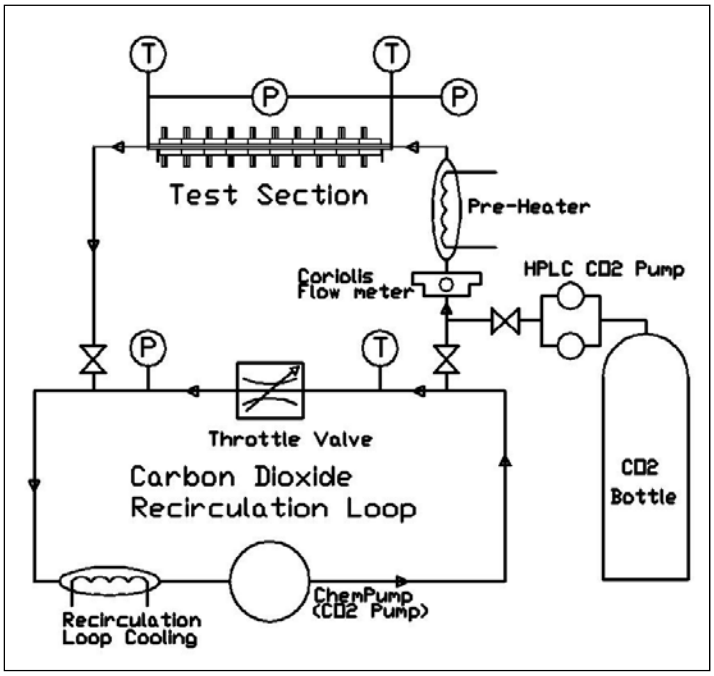

Figure 3.1: Schematic of the experimental facility at University of Wisconsin at Madison [4]

The CO_2 recirculation loop consists of ChemPump capable of flow rates up to $14m^3/hr$, dynamic head of 15 m and pressure drop of 20MPa.This pump generates a pressure drop across the throttle which drives the flow into the test section. The absolute pressure of the recirculation loop is monitored with a Siemens pressure transducer (Model 7MF4432-1GA10-1NC1-Z), which is recorded during experiments and has operating limits of 0-40MPa, with and an accuracy better than 0.1%. One K-type thermocouple was installed to monitor loop temperature, which was calibrated within 0.1^oC over the range of $5\text{-}75^oC$. From the CO_2 loop, flow is directed to the heat transfer loop. The flow rate is measured accurately with a Siemens Coriolis flow meter (Sitrans FC Massflow-Mass 2100), which has a flow range from 0-250kg/hr and error of less than 0.1%. Directly after the flow meter the CO_2 is pre- heated and then proceeds into the heat exchanger test section, where pressure drop is measured by a differential pressure transducer (Model 7MF4032-1GA10-1NC1-Z). All heating and pressure systems were monitored, recorded, and controlled by Labview software [4].

The heat exchanger test section consists of several components. On the heat transfer section nine parallel channels are etched onto 316 stainless steel plates as shown in Figure 3.2. The channel length is half meter, with each channel being a semi-circle with a diameter of 1.9mm.

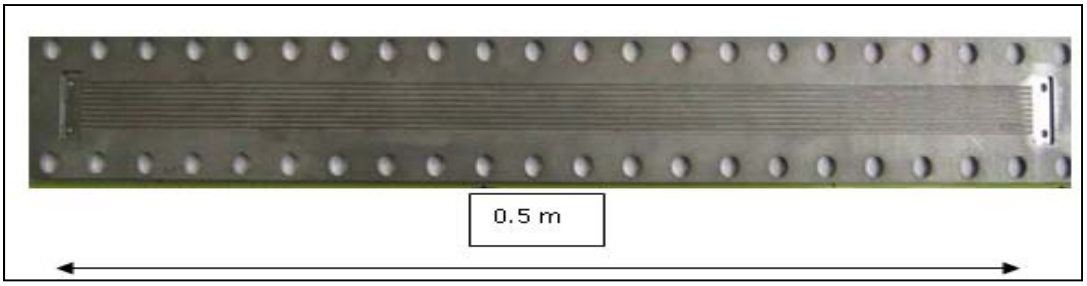

Figure 3.2: Heat exchanger test section at University of Wisconsin-Madison [4]

CHAPTER IV

MODELING PROCEDURE

This section discusses the governing equations, and the methods of solution to model the convective heat transfer and turbulence in Sc-CO_2. A numerical approach is taken to model this problem. The numerical modeling consists of construction of a mathematical description of the object to be modeled, deriving a set of differential/integral equations, discretizing these equations into system of algebraic equations using a Finite-Volume discretization technique to obtain the solution.

FLUENT, which is the commercially available computational fluid dynamics tool is used. It uses the finite volume technique to obtain the solution. This technique approximates the governing equations over a volume. For all flows FLUENT solves the continuity and the momentum equation. For the problem under consideration heat transfer is involved so an additional energy equation is solved. The flow is highly turbulent; the k-ε model with enhanced wall conditions and k-ω SST model are used for turbulence, which solves the kinetic energy and the dissipation equations.

There is no single turbulence model that can resolve the physics at all flow conditions. FLUENT provides a wide variety of models to suit the demands of individual classes of problems. The choice of the turbulence model depends on the required level of accuracy, available computational resources, and the required turnaround time. The key features of the two turbulent models used in the present work are described in Table 4.1.

Table 4.1: Description of the turbulent models

Turbulent Model	Description
Realizable k-ε model	Recommended for flows with boundary layers under strong adverse pressure gradient, separation and recirculation.
SST k- ω model	Behaves like k- ω model in the near wall region and like standard k-ε in the free stream. It is more accurate and reliable for a wider class of flows

4.1 Governing equations

The mass conservation equation at steady state condition is used in this problem.

$$\frac{\partial}{\partial \mathrm{t}}(\rho u_i) + \frac{\partial}{\partial \mathrm{x_i}}(\rho u_i) = 0 \tag{4-1}$$

For turbulent flows, by using the Reynolds time averaging method, the momentum equation results to:

$$\frac{\partial}{\partial \mathrm{t}}(\rho u_i) + \frac{\partial}{\partial \mathrm{x_i}}\left(\rho u_i u_j\right) = \rho g_i - \frac{\partial P}{\partial x_j} + \frac{\partial \tau_{ij}}{\partial x_j} + \frac{\partial}{\partial \mathrm{x_j}}\left(-\rho\overline{u_i' u_j'}\right) \tag{4-2}$$

Where τ_{ij} is the shear stress given by

$$\tau_{ij} = \mu\left(\frac{\partial u_i}{\partial x_j} + \frac{\partial u_j}{\partial x_i} - \frac{2}{3}\delta_{ij}\frac{\partial u_k}{\partial x_k}\right) \tag{4-3}$$

The Boussinesq hypothesis is used to relate the Reynolds stresses to the mean velocity gradients. This approach is used in the *k-ε* and *k-ω* of turbulence.

$$-\rho\overline{u_i' u_j^i} = \mu_t\left(\frac{\partial u_i}{\partial x_j} + \frac{\partial u_j}{\partial x_i} - \frac{2}{3}\delta_{ij}\frac{\partial u_k}{\partial x_k}\right) - \frac{2}{3}\delta_{ij}\rho \tag{4-4}$$

The symbols with primes denote the fluctuating components of the corresponding quantities. This type of modeling is called the eddy viscosity modeling [6].

k-ε Realizable model

The turbulent viscosity for the realizable *k-ε* is given by:

$$\mu_t = \rho C_\mu \frac{k^2}{\varepsilon} \tag{4-5}$$

C_μ is not a constant unlike the standard and the RNG *k-ε* models. The transport equations for turbulent kinetic energy (k) and the rate of its dissipation ε are given by the following equations:

$$\frac{\partial(\rho k \mu_j)}{\partial x_j} = \frac{\partial}{\partial x_j}\left[\left(\mu + \frac{\mu_t}{\sigma_k}\right)\frac{\partial k}{\partial x_j}\right] + G_k + G_b - \rho\varepsilon - Y_M + S_k \tag{4-6}$$

$$\frac{\partial(\rho \varepsilon \mu_j)}{\partial x_j} = \frac{\partial}{\partial x_j}\left[\left(\mu + \frac{\mu_t}{\sigma_\varepsilon}\right)\frac{\partial \varepsilon}{\partial x_j}\right] + \rho C_1 S\varepsilon - \rho C_2 \frac{\varepsilon^2}{k+\sqrt{\varepsilon}\vartheta} + C_{1\varepsilon}\frac{\varepsilon}{k} C_3 G_b + S_\varepsilon \tag{4-7}$$

Here G_k represents the generation of turbulence kinetic energy due to the mean velocity gradients given by

$$G_k = \mu_t S^2 \tag{4-8}$$

where S is the modulus of the mean rate-of-strain tensor given by:

$$S = \sqrt{2 S_{ij} S_{ij}} \tag{4-9}$$

G_b is the generation of turbulent kinetic energy due to buoyancy given by

$$G_b = \beta \frac{\mu_t}{Pr_t} \underline{g}.\nabla T \tag{4-10}$$

where Pr_t is the turbulent Prandtl number which is 0.85 for this model and g_i is the gravity in the ith direction. Y_M is the contribution of fluctuation dilation for compressible turbulence to the overall dissipation rate. This is given by

$$Y_M = 2\rho\varepsilon M_t^2 \tag{4-11}$$

$$M_t = \sqrt{\frac{k}{a^2}} \tag{4-12}$$

$$a = \sqrt{\gamma RT} \tag{4-13}$$

C_2 and $C_{1\varepsilon}$ are constants. σ_k and σ_ε are the Prandtl numbers for the k and ε. S_k and S_ε are the ω user-defined source terms [6].

<u>*k-ω SST* model</u>

This model behaves like a k-omega model in the near wall region and k-epsilon in the free stream. These two models are blended using a blending function. This model is suitable for flows having adverse pressure gradients, shocks and waves. The model transport equations are as follows:

$$\frac{\partial(\rho k\mu_j)}{\partial x_j} = \frac{\partial}{\partial x_j}\left[\Gamma_k \frac{\partial k}{\partial x_j}\right] + G_k - Y_k + S_k \tag{4-14}$$

$$\frac{\partial(\rho \omega\mu_j)}{\partial x_j} = \frac{\partial}{\partial x_j}\left[\Gamma_\omega \frac{\partial \omega}{\partial x_j}\right] + G_\omega - Y_\omega + D_\omega + S_\omega \tag{4-15}$$

Here G_k represents the generation of turbulence kinetic energy due to mean velocity gradients evaluated as (equation number), G_ω represents the generation ofω. Γ_k and Γ_ω represent the effective diffusivity of k and ω. Y_k and Y_ω is the dissipation of k and ω, D_ω is the cross diffusion source term and S_k and S_ω are the user defined source terms [6].

The energy equation in terms of enthalpy is of the form

$$\frac{\partial}{\partial \mathrm{x_i}}(\rho u_i H) = \frac{\partial}{\partial x_i}\left(\lambda \frac{\partial T}{\partial x_i} + \frac{\mu_t}{Pr_t}\frac{\partial H}{\partial x_i}\right) - u_i \frac{\partial P}{\partial x_i} + + \dot{\mathrm{Q}} + \emptyset \tag{4-17}$$

The Bossinesque assumption has been used to model the turbulent heat flux.

$$\varphi = \left(\frac{\partial u_i}{\partial x_j} + \frac{\partial u_j}{\partial x_i} - \frac{2}{3}\delta_{ij}\frac{\partial u_k}{\partial x_k}\right)\frac{\partial u_i}{\partial x_j} \tag{4-18}$$

To calculate the heat transfer coefficient the following equations are used:

$$h[j] = \frac{q_w[j]}{T_w[j] - T_b[j]} \tag{4-19}$$

T_w is the average circumferential wall temperature and the heat flux is given by the following equation:

$$q_w[j] = \frac{\dot{m}(i_b[j]-i_b[j-1])}{A_w[j]} \quad (4\text{-}20)$$

$$A_w = r(2+\pi)dz \quad (4\text{-}21)$$

Where d is the tube diameter (1.9mm), and dz is the length between cross sectional slices. The bulk enthalpy at each cross section is calculated by the following equation:

$$i_b = \frac{\int \rho w i dA_c}{\int \rho w dA_C} \quad (4\text{-}22)$$

$$T_b = \frac{\int \rho w T dA_c}{\int \rho w dA_C} \quad (4\text{-}23)$$

Where ρ is the density, w is the velocity, i is the enthalpy and P is the system pressure at each volumetric cell for a given axial location, dA_c is the cross sectional area of each cell. The heat transfer calculations are done via a User Defined Function.

4.2 Universal law of the wall

The velocity distribution in the boundary layer can be divided into three regions starting at the wall: the viscous sub-layer, the buffer region and the log region. Resolving the flow to the viscous sub-layer becomes very important which makes the near wall modeling important. Some of the commonly used non-dimensionless parameter are defined as follows:

The non-dimensional velocity u+ is evaluated as:

$$u^+ = \frac{u}{u_\tau} \quad (4\text{-}24)$$

Where u_τ is the friction velocity.

$$u_\tau = \sqrt{\frac{\tau_w}{\rho}} \tag{4-25}$$

where τ_w is the shear stress at the wall and ρ is the density of the flow. The non-dimensional distance to the wall y+ is

$$y^+ = \frac{\rho u_\tau y}{\mu} \tag{4-26}$$

In the viscous sub-layer the velocity profile is linear and is described by

$$u^+ = y^+ \tag{4-27}$$

In the log region, the turbulent effects dominate and the velocity profile follows a logarithmic profile

$$u^+ = \frac{1}{k} ln(y^+) + C \tag{4-28}$$

Where k is the von Karman constant 0.4187 and C is found to be 5.45

The buffer region is effected both by the laminar and turbulent effects. The velocity transitions from a linear to a logarithmic profile. The velocity profile with both mentioned asymptotes is shown in a semi-logarithmic Figure 4.1.

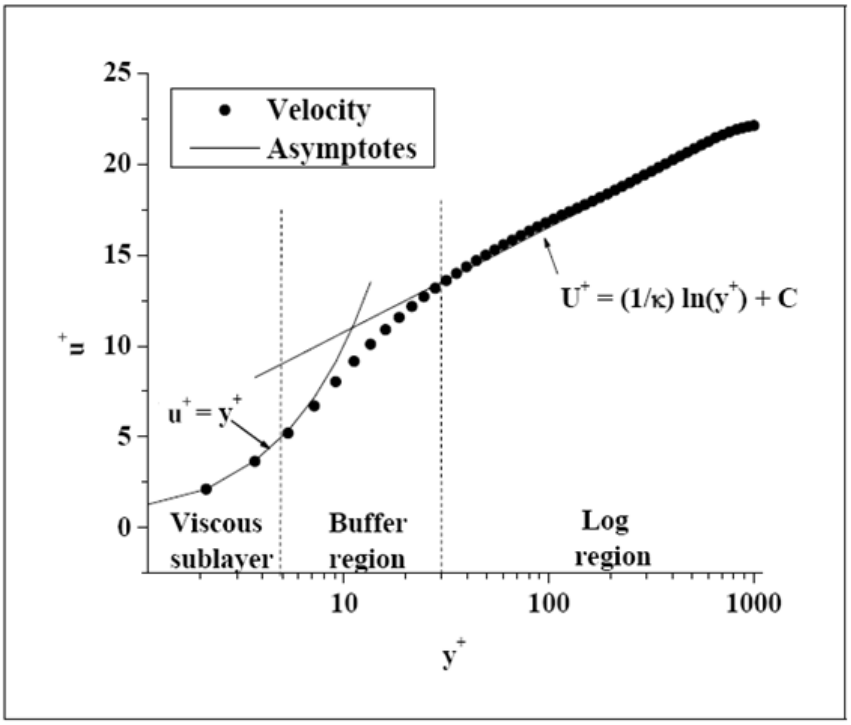

Figure 4.1: Dimensionless near wall velocity profile [6]

4.3 Wall modeling

In any numerical solution the near wall modeling plays a significant role. It is the near wall regions that the solution variables have large gradients, momentum and other scalar transports occur very rigorously. There are two approaches in modeling the near-wall region. In one approach the viscosity affected region is resolved with the mesh all the way to the wall, including the viscous sub-layer. The enhanced wall treatment combines the two-layer model with enhanced wall functions. This approach requires the near-wall mesh to be fine enough to resolve the laminar sub-layer increasing the computational time. In another approach the viscous sub-layer is not resolved. There are

semi-empirical formulas called wall functions which bridge the viscous sub-layer to the bulk region. The two turbulent models k-ϵ realizable with enhanced wall treatment and k-ω SST will be used in this problem. Figure 4.2 shows this approaches discussed above.

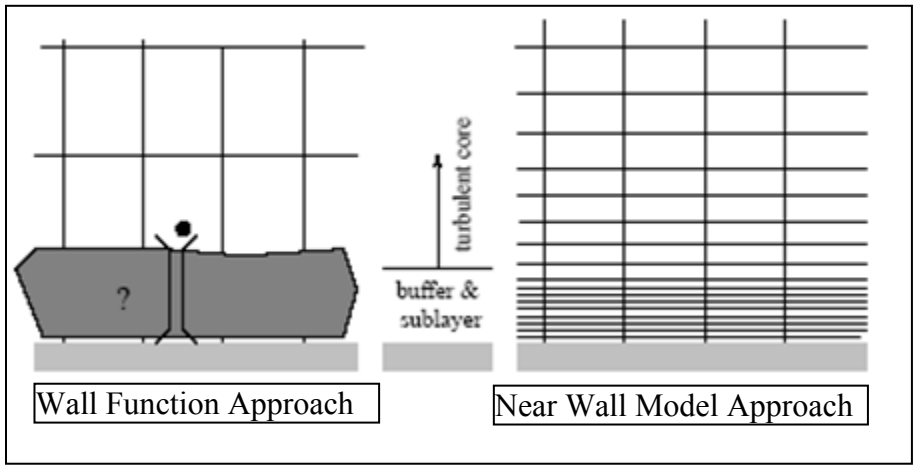

Figure 4.2: Near wall treatment in FLUENT [6]

CHAPTER V

SOLUTION METHOD

5.1 Computational geometry

The approach taken here is to computationally investigate the flow and heat transfer for three different geometries – a single semi-circular channel of diameter 1.9mm, a series of nine parallel semi-circular channels each of diameter 1.9 mm and a single zig-zag channel. In the experimental setup these channels are etched in a rectangular plate, the dimensions of which are shown in Figure 5.1. The cross section of the plate is 66mm by 6.3mm as shown in Figure 5.1. The channels, be it a single channel or a series of nine channels or a zig-zag channel, are embedded in a steel structure as shown in Figure 5.2. The entire geometry is extruded to a length of 500 mm. A three dimensional model of these geometries was generated using GAMBIT (version 2.4.6) and various meshes were generated to study the problem.

The cross-sectional view of the single channel and nine channel computational domains are shown in Figures 5.3 and 5.4, respectively. The single channel case will from hereon be referred to as case 1; while the nine channels case will be referred to as case 2, in the for future discussion. The computational model for the zigzag channel is similar to that shown for semi-circular channel. The geometry of one segment of the zigzag channel is shown in Figure 5.5.

The inlets and outlets of the test section are shown in Figure 5.2. A constant mass flux and a fixed temperature are specified at the inlet. The inlet of the problem is fixed as

a mass flow inlet boundary condition. A pressure boundary condition is specified at the outlet. The experimentally measured temperatures on the surface of the top and the bottom walls of the test section at different axial locations are used as fixed temperature boundary condition. All the other external surfaces are assumed to be insulated i.e. have zero heat flux. The NIST Standard Reference database is used for the temperature and pressure dependent thermal properties of CO_2 [21]. The test section is operated at a certain high pressure and the buoyancy effects due to gravity are also included in the thermal models.

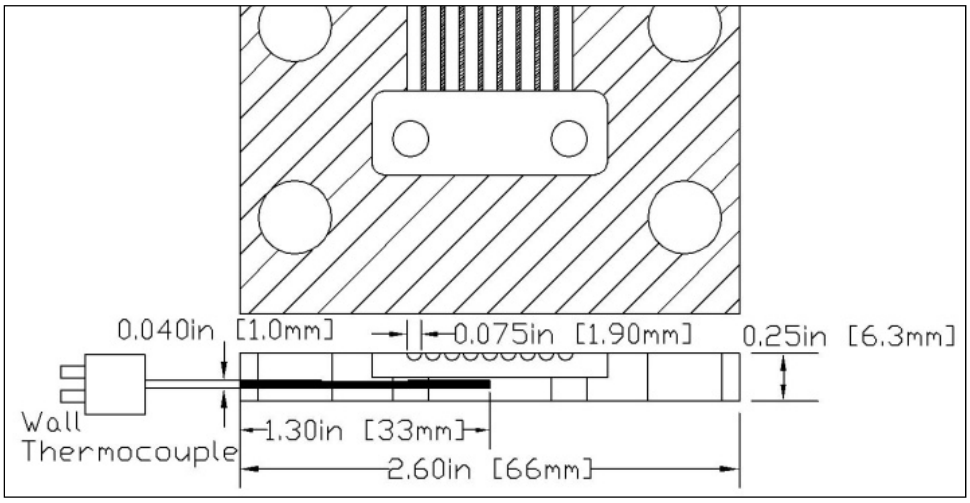

Figure 5.1: Dimensions of the test section [4]

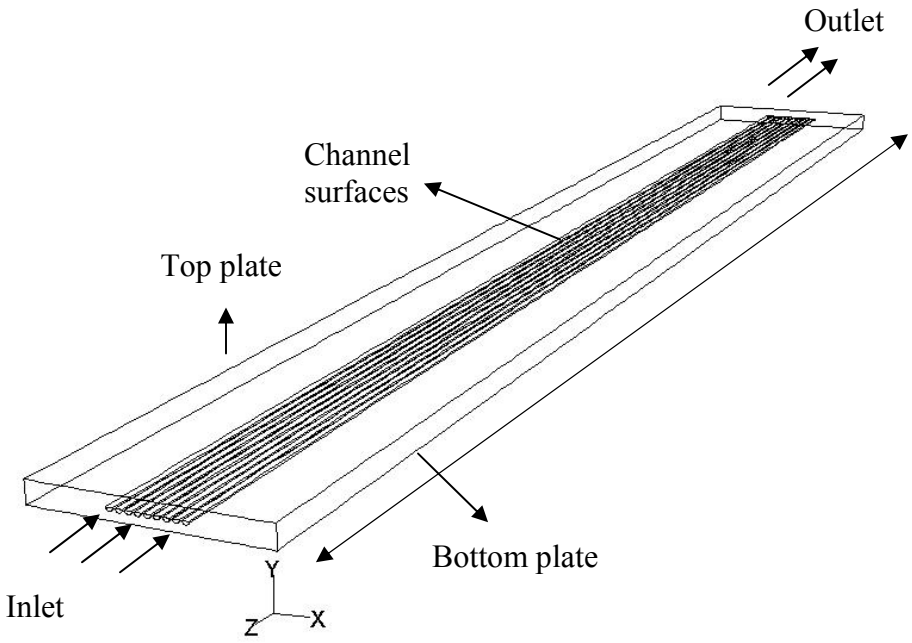

Figure 5.2: Geometry details for case 2

0.5 m

Figure 5.3: Single semi-circular geometry

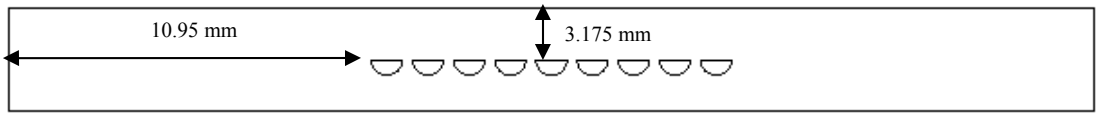

Figure 5.4: Nine semi-circular channels geometry

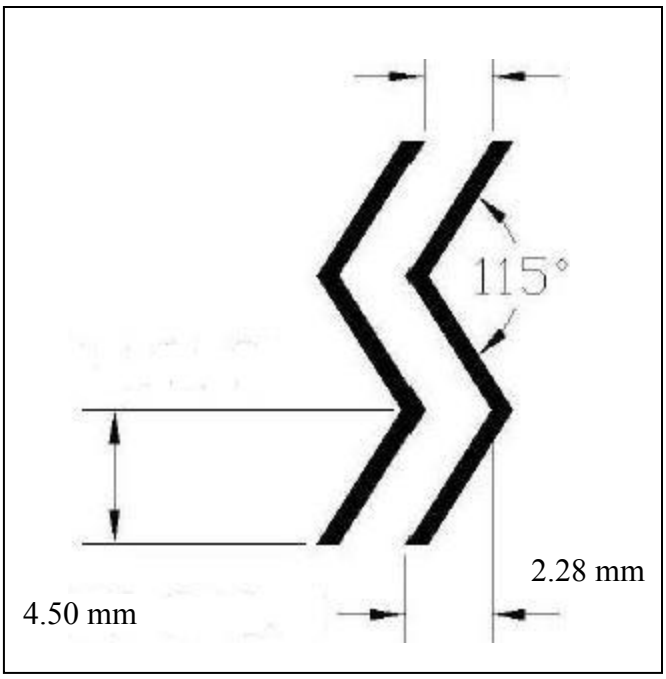

Figure 5.5: Specific zig-zag channel geometry

All the simulations evaluated and documented in this thesis are performed using a second order finite volume commercial code FLUENT (Version 12.0). The physics of the problem is governed by the famous three dimensional mathematical equations referred to as the Navier Stokes equations. These governing equations are solved in a three-dimensional cartesian system. The Finite Volume (FV) method is used to discretize these equations up to second order of spatial accuracy. Two different turbulence models - realizable k-ε and k-ω SST models are used to model the turbulent nature of the flow inside the channels. The pressure-based solver in FLUENT which solves for mass, momentum and the energy equation is used. This solver uses the pressure-based approach; the pressure equation is derived from the continuity and the momentum equations, in such a way that the velocity field corrected by the pressure

satisfies the continuity. SIMPLE algorithm is used for pressure and velocity coupling.

The second order UPWIND scheme is used to approximate all the transport equations. In this scheme the quantities at cell faces are computed using a multidimensional linear reconstruction approach [22]. In this approach, higher-order accuracy is achieved at cell faces through a Taylor series expansion of the cell-centered solution about the cell centroid. Thus when second-order upwinding is selected, the face value φ_f is computed using the expression below:

$$\varphi_{f,SOU} = \varphi + \nabla\varphi.r \tag{5.1}$$

where φ and ∇□ are the cell-centered value and its gradient in the upstream cell, and $\vec{r}$ is the displacement vector from the upstream cell centroid to the face centroid. This equation requires the determination of the gradient ∇□ in each cell. This is evaluated using the Green-Gauss Node based gradient evaluation.

The Green-Gauss approach uses the following equation for evaluation of the gradient at the cell center:

$$\nabla\varphi = \frac{1}{v}\sum_f \overline{\varphi_f}\,\overline{A_f} \tag{5.2}$$

where $\overline{\varphi_f}$ is evaluated using the Green-Gauss node based approach:

$$\overline{\varphi_f} = \frac{1}{N_f}\sum_n^{N_f} \overline{\varphi_n} \tag{5.3}$$

where N_f is the number of nodes on the face. The nodal values φ_n is constructed from the weighted average of the cell values surrounding the nodes following the approach originally proposed by Holmes and Connel and Rauch et al [23]. This scheme reconstructs exact values of a linear function at a node from surrounding cell-centered

values on arbitrary unstructured meshes by solving a constrained minimization problem, preserving a second-order spatial accuracy.

The under relaxation parameters are chosen such that the oscillatory solution is avoided and relatively faster convergence rate is obtained.

The steady state simulations were carried out for all three different cases with pressures as high as 7.5MPa and 8.1MPa for different inlet temperatures and mass fluxes. To carry out these studies, mesh sensitivity and convergence studies were carried out to assess numerical errors. More details on the mesh generation are discussed in the next section.

5.2 Mesh study

It is required to detect, estimate and control numerical uncertainty/or error in CFD studies. In order to capture the flow details, a good mesh is required. However, it is unrealistic to use a mesh which is too large since it will dramatically increases the computational time. So grid and accuracy refinement studies are carried out to assess the associated numerical errors.

Figures 5.6 and 5.7 show the mesh generated for the flow inside the semi-circular channels (case 1 and case 2) and on the surface of a segment of zigzag channel, respectively. Since the flow inside the channel is turbulent in nature, it is highly desirable to resolve the near wall mesh to a significant detail in order to capture the physics of the flow accurately. Henceforth, it can be seen in Figures 5.6 and 5.7 that the mesh is clustered near the channel walls. In order to avoid expensive computational simulation time, a relatively coarser mesh is generated for the steel structure i.e., outside

the channel. Figures 5.8 and 5.9 show the cross sectional view of the meshed geometry of a single channel and a series of nine channels, respectively.

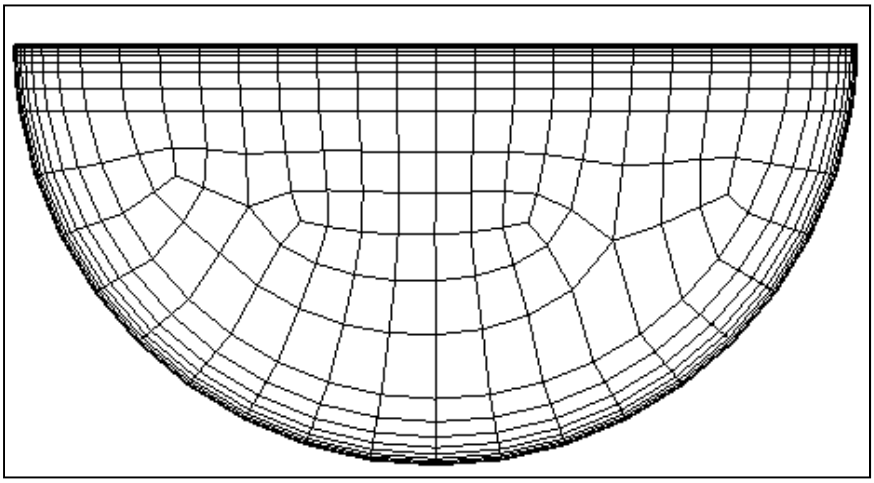

Figure 5.6: Grid details inside the semi-circular channel

Three meshes were generated for case 1 and 2, each varying in the number of cells. The number of cells used in each of the meshes is listed in the table below. In order to resolve most of the flow details it is essential to place the first node of the mesh in the viscous sub-layer region. This requires that the dimensionless distance normal to the wall y^+ <1. All the meshes generated had a y^+<1. Each mesh differed in the aspect ratio of the cells.

It is recommended to study the grid convergence and grid independence study when dealing with CFD problems. A grid convergence study is carried out using the course, fine and finest meshes as illustrated in the table below. It evaluates the

discretisation error in the CFD solution. It verifies if the solution of the problem is done on a sufficiently fine grid resolution.

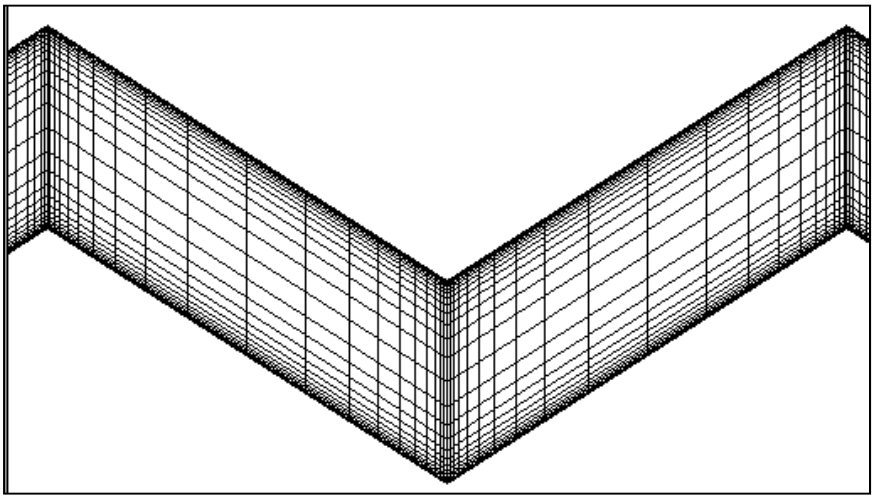

Figure 5.7: Grid details for a segment of the zigzag channel

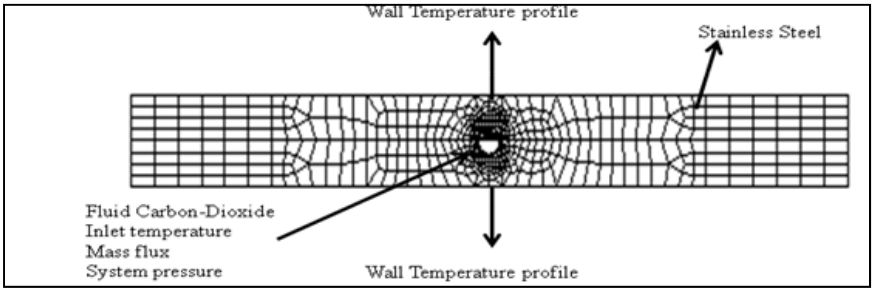

Figure 5.8: Meshed geometry of a single channel

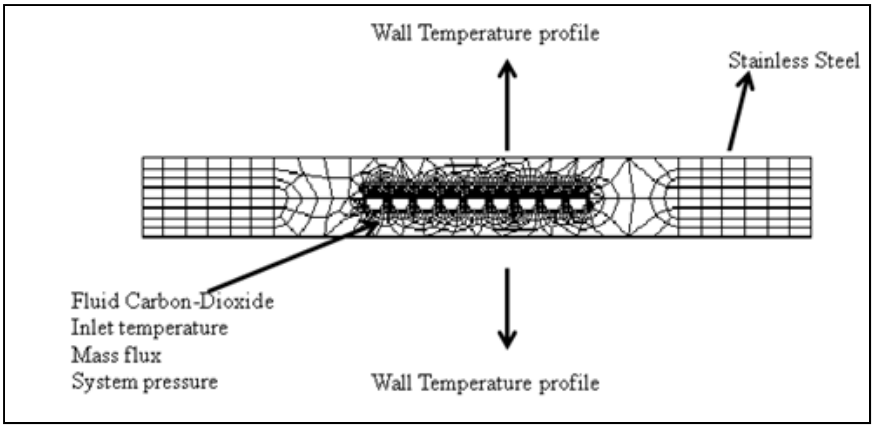

Figure 5.9: Meshed geometry with nine channels

Table 5.1: Number of cells in coarse, fine and finest meshes

Mesh Type	CASE 1 (Single Channel) Number of Cells	CASE 2 (Nine Channels) Number of Cells
Coarse	127,000	746,000
Fine	254,000	895,000
Finest	746,000	1,116,000

The following sets of equations are used to evaluate the grid convergence index (GCI). Select three different sets of grids, and run simulations to determine the key variable φ important to the objective of the simulation study. Here heat transfer coefficient is the key variable. The three dimensional calculation of the mesh or grid size is given by [24]:

$$h = \left[\frac{1}{N}\sum_{i=1}^{N}\Delta V_i\right]^{\left(\frac{1}{3}\right)} \tag{5-4}$$

This parameter is calculated for the three meshes, the grid refinement factor is evaluated using the following equation:

$$r = \frac{\mathrm{h_{course}}}{\mathrm{h_{fine}}} \tag{5-5}$$

Calculate the extrapolated values using equation below:

$$\varphi_{ext}^{21} = \frac{(r_{21}^{p}\varphi_1 - \varphi_2)}{r_{21}^{p} - 1} \tag{5-6}$$

Where φ_1 is the heat transfer coefficient for course mesh and φ_2 for the fine mesh. The approximate relative error is found between the key variable of the two meshes.

$$e_a = \left|\frac{\varphi_1 - \varphi_2}{\emptyset_1}\right| \tag{5-7}$$

The extrapolated relative error is evaluated using

$$e_{ext}^{21} = \left|\frac{\varphi_{ext}^{21} - \varphi_2}{\varphi_{ext}^{21}}\right| \tag{5-8}$$

The GCI is calculated using

$$GCI_{fine}^{21} = \frac{1.25 e_a^{21}}{r_{21}^{p} - 1} \tag{5-9}$$

The next chapter discusses the results of heat transfer coefficient obtained using various meshes. It also discusses a detailed analysis of grid independent study carried out for the various meshes. The grid convergence index is the factor which establishes whether the solution obtained using a mesh is grid independent.

CHAPTER VI

RESULTS AND DISCUSSION

6.1 Single channel geometry

A simulation is carried out for case 1, at an inlet temperature of 14.99°C and a pressure of 7.5MPa with a mass flux of 761.94 kg/m^2-s in the heating mode. The wall temperature on the top and bottom at various axial locations which is a boundary condition is shown in Table 6.1.

Table 6.1: Temperatures measured experimentally at the top and bottom wall

Axial (mm)	25	75	125	175	225	275	325	375	425	475
Tw_Top	30.5	31.8	33.2	33.9	34.5	35.4	35.2	35.5	35.8	36.2
Tw_Bottom	33.4	35.3	37.0	36.4	37.5	36.8	38.6	38.5	38.5	38.1

This simulation was chosen for the numerical study because according to the experiments for these operating conditions, the fluid passes through the pseudocritical temperature at some axial location. The physics of Sc fluids in the pseudocritical region can be best studied in this case. Grid convergence studies are carried out with the input parameters just mentioned. Also, the simulations are carried out with two different turbulent models - the k-ε realizable model with enhanced wall treatment and the k-ω SST model; in order to choose the appropriate one for this problem. The results of these

evaluations are presented in Tables 6.2 and 6.3. The heat transfer coefficient of the problem is calculated for all the meshes (Table 6.2) using the *k-ε* realizable turbulence model to determine the optimum grid for this problem and study the grid convergence. A similar study is performed with the *k-ω* SST model and the results are tabulated in Table 6.3.

Table 6.2 suggests that the heat transfer coefficient for coarse, fine and finest meshes is similar. Therefore, it can be concluded that a grid independent solution is obtained and further grid refinement is not required. The heat transfer coefficient determined for three different meshes are used to calculate the grid convergence index based on the methodology described in Chapter V. Table 6.4 shows the GCI values calculated for the three meshes used to study the grid convergence. According to Table 6.4, the numerical uncertainty in the finest grid solution for the heat transfer coefficient is only 3.1%. The GCI values reduce with grid refinement thereby suggesting grid convergence is obtained.

Table 6.2: Heat transfer coefficient evaluated for the single channel geometry using the k-ε realizable turbulence model

Mesh Type	Mesh Size (No. of Cells)	HTC-Numerical [W/m^2-K]	HTC-Experimental [W/m^2-K]
Coarse	127,000	4964.5	7184
Fine	254,000	5042.5	
Finest	746,000	5005.0	

Table 6.3: Comparison of heat transfer coefficient for the single channel geometry using different turbulence models

Turbulence Model	Mesh Size (No. of Cells)	HTC-Numerical [W/m^2-K]	HTC-Experimental [W/m^2-K]
k-ε realizable	127,000	4964.5	7184
k-ω SST model	127,000	4038.9	

Table 6.4: Grid convergence calculations

Variable Name	Values
r_{21}	0.7937
r_{32}	0.6980
$\emptyset_1$	4964.5
$\emptyset_2$	5042.5
$\emptyset_3$	5005.0
e_a^{21}	1.57%
e_a^{32}	0.743%
e_{ext}^{21}	1.52%
e_{ext}^{32}	1.76%
GCI_{21}	9.5%
GCI_{32}	3.1%

Since the heat transfer coefficient remains essentially unchanged with grid refinement, coarse mesh is used for further evaluations to reduce computational cost. A

study on turbulent models is provided in Table 6.3. The result suggests that *k-ε* realizable turbulent model with enhanced wall treatment results in slightly better agreement with the experiment value. Therefore, all further calculations are performed with the coarse mesh and *k-ε* realizable turbulent model for the single channel case.

The variation of heat transfer coefficient with the dimensionless bulk mean temperature T_b/T_{pc} of the fluid under the condition specified at the beginning of this section is shown in Figure 6.1. It is a known from theory that under certain conditions there is an enhancement in heat transfer when the pseudocritical temperature is equal to the bulk temperature. The numerical results predict enhancement in heat transfer in this simulation, assuring the validity of the results.

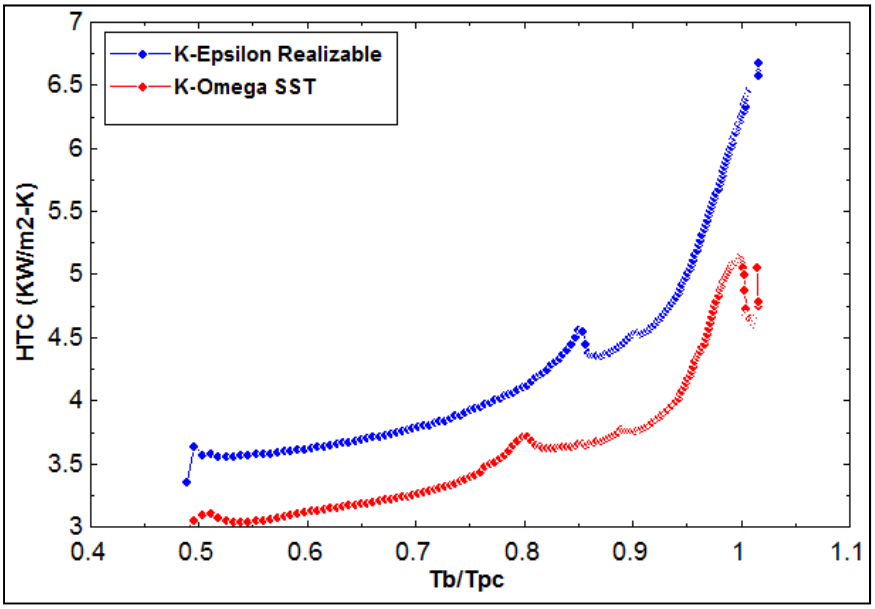

Figure 6.1: Numerical results - heat transfer coefficient in the single channel case at M=761.94 kg/m^2-s, T_{in}=14.99^{o}C, P_{op}=7.5MPa

The variation in the specific heat and the density of Sc-CO_2 is computed with varying bulk temperature and is shown in Figure 6.2. This variation in properties make the heat transfer of Sc-CO_2 very different from conventional fluids. There is a peak in the specific heat capacity in the pseudocritical region while the density drops in this region. This peak in the specific heat is one of the reasons for the increase in the heat transfer coefficient in the pseudocritical region

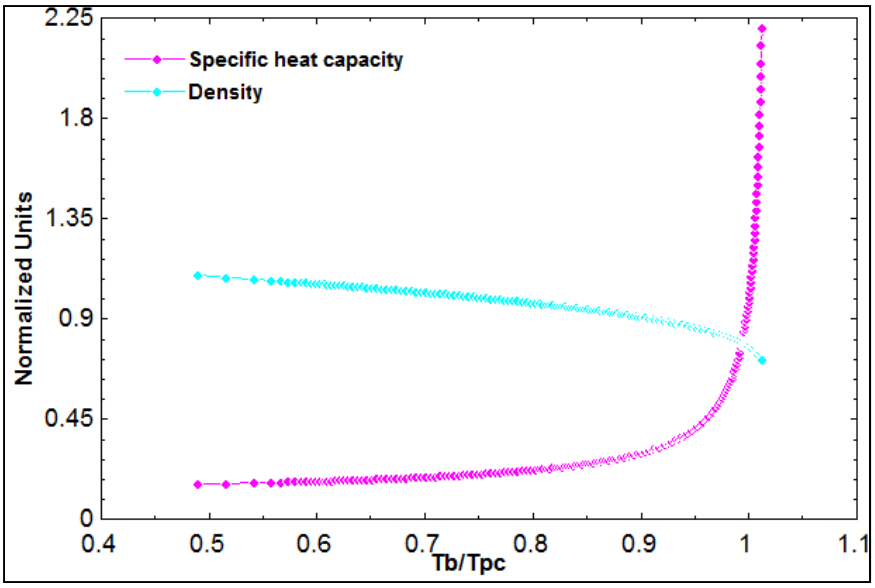

Figure 6.2: Variation of specific heat and density in the single channel case at M=761.94 kg/m^2-s, T_{in}=14.99^{o}C, P_{op}=7.5MPa

The variations of Prandtl number Pr_b and Reynolds number Re_b with the bulk temperature for the inlet conditions specified at the beginning of this section are shown

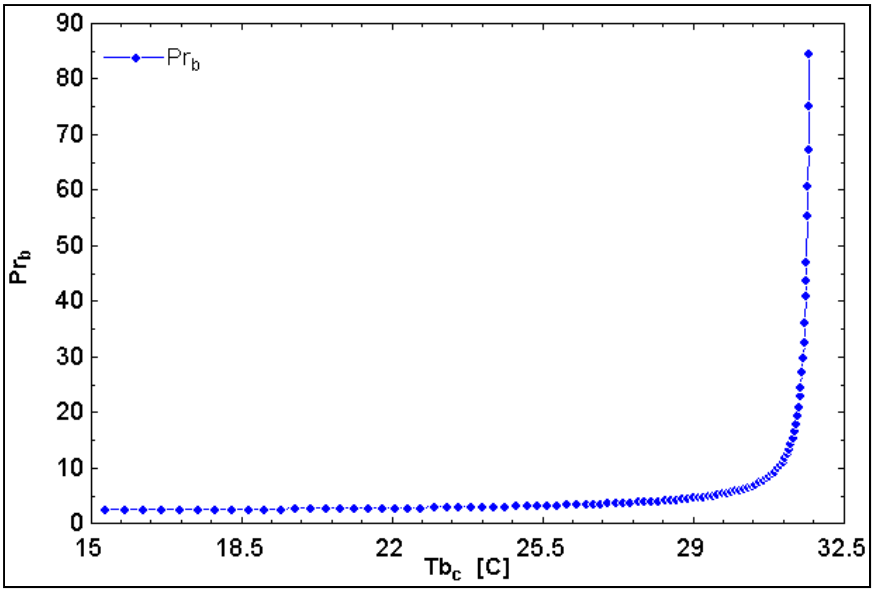

Figure 6.3: Variation of Prandtl number with bulk temperature for the single channel case at M=761.94 kg/m^2-s, T_{in}=14.99^{o}C, P_{op}=7.5MPa

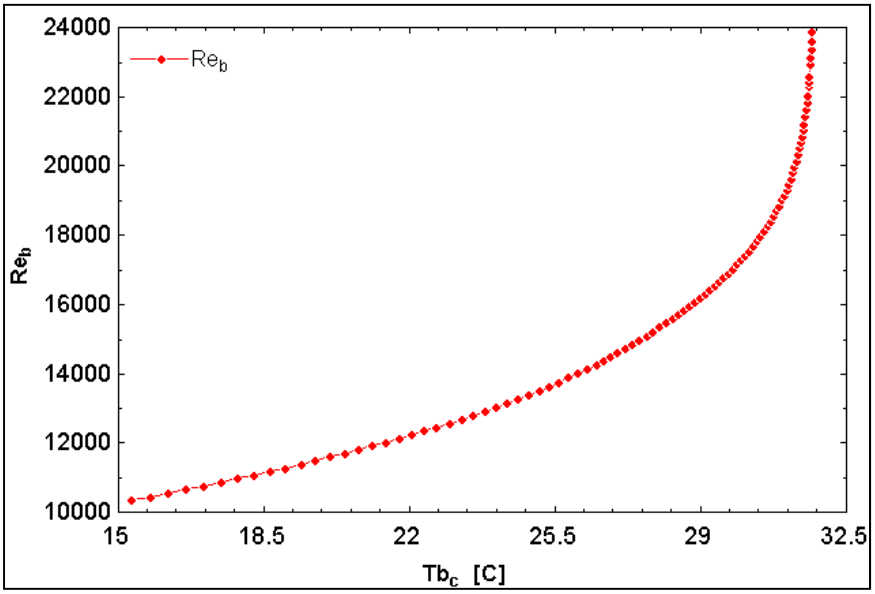

Figure 6.4: Variation of Reynolds number with bulk temperature for the single channel case at M=761.94 kg/m^2-s, T_{in}=14.99^{o}C, P_{op}=7.5MPa

in Figures 6.3 and 6.4 respectively. The results clearly indicate the peak when the bulk temperature approaches the pseudocritical temperature.

A study of the variation of heat transfer coefficient was made along the axial direction of the channel and is plotted in Figure 6.5. A good agreement in the heat transfer coefficient is observed between the two turbulence models. However, the heat transfer coefficient calculated from the experiments is higher than the numerical values. The factors that affect the heat transfer coefficient are the bulk temperature, the wall temperature and bulk enthalpy. Since the wall temperature is an input to the simulation (obtained from the experiments), the factors that might be responsible for differences between the simulation and the experiment are restricted to fluid bulk temperature and bulk enthalpy. Therefore, the bulk enthalpies and bulk temperature need to be investigated. The bulk enthalpy is obtained from the bulk temperature and the pressure, therefore investigating the bulk temperatures will be sufficient (Chapter IV).

A comparison of the numerical and experimental results of bulk temperature is made and shown in the Figure 6.6. It is observed from the figure that the bulk temperature calculated using the k-ε and the k-ω models is in an excellent agreement with the experiments. The experimental heat transfer coefficient values presented so far were measured for a test section with nine channels. The numerical simulation results for the single channel are however compared with these experiment results to understand the effect of having multiple micro-channels in the test section. The probable reason for the numerical and experiment results to differ from each other could be the heat transfer phenomenon between the channels which is missing in the single channel case. The heat

transfer coefficient in a single channel case is predicted lower than the experiments (carried out in the actual test section consisting of nine channels). Since Sc-CO_2 enhances heat transfer, the nine channel case has a higher heat transfer coefficient than a single channel. The single channel case, however, could not provide a concrete conclusion other than the appropriate mesh and turbulent model to be used for numerical computations. This problem needs further investigation by modeling the nine channel geometry. Numerical simulations need to be carried out for this case and compared with the experiments.

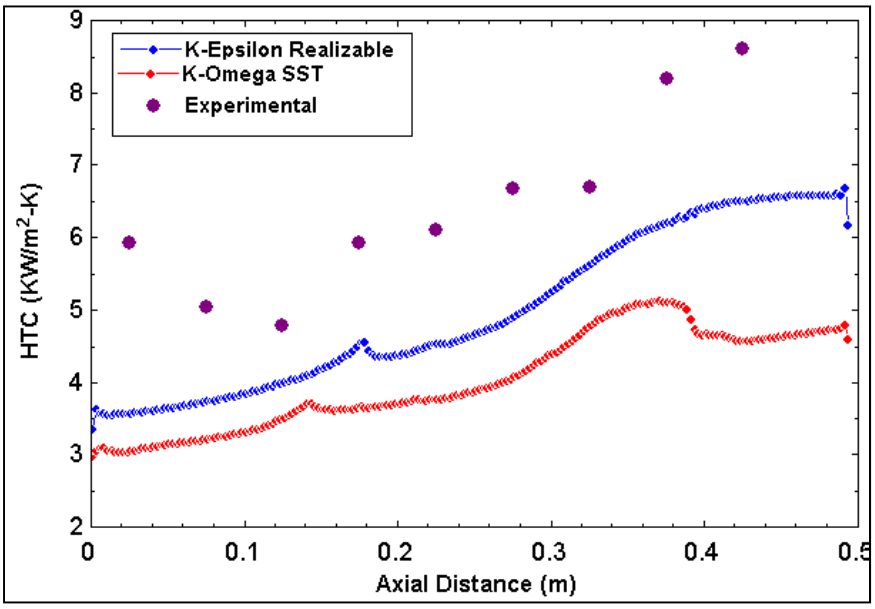

Figure 6.5: Axial variation of heat transfer coefficient for the single channel case at M=761.94 kg/m^2-s, T_{in}=14.99^{o}C, P_{op}=7.5MPa

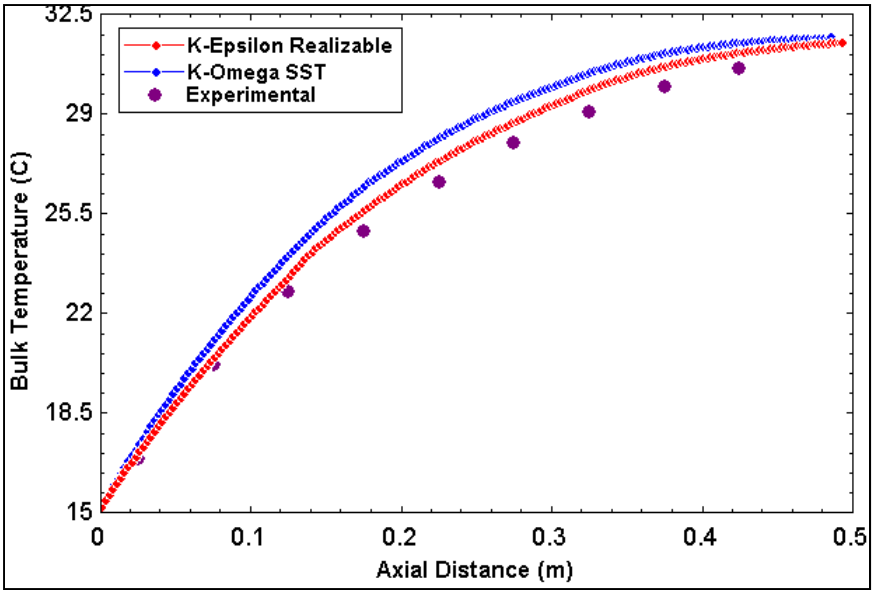

Figure 6.6: Axial variation of bulk temperature for the single channel case at M=761.94 kg/m^2-s, T_{in}=14.99^{o}C, P_{op}=7.5MPa

6.2 Series of nine semi-circular channels

A numerical simulation is carried out for the nine channel geometry with inlet CO_2 temperature of 14.99°C and an operating pressure of 7.5MPa with a mass flux of 761.94 kg/m^2-s. The problem is setup in the heating mode and computations are performed on three different meshes using two turbulence models - *k-ε* realizable turbulence model with enhanced wall treatment and *k-ω* SST turbulence model.

The results of these evaluations are presented in Tables 6.5 and 6.6. The heat transfer coefficient of this problem is calculated for all the meshes (Table 6.5) using the *k-ε* realizable turbulence model to determine the optimum grid for this problem and study the grid convergence. It is observed that the heat transfer coefficient for coarse,

fine and finest meshes is similar confirming the grid convergence and accuracy of the model.

Table 6.5: Comparison of heat transfer coefficient using the k-ε realizable model

Mesh Type	Mesh Size (No. of cells)	HTC-Numerical [W/m^2-K]	HTC-Experimental [W/m^2-K]
Coarse	746,000	12917.1	7184
Fine	895,000	12622.0	
Finest	1,119,000	12623.6	

A similar study is performed with the *k*-*ω* SST model under the same operating conditions and the results are tabulated in Table 6.7. The heat transfer coefficient for all the meshes is calculated and is found to be similar for all. Thus further mesh refinement is not required and coarse mesh can be used for further evaluations to reduce computational cost. The results reported in Tables 6.6 and 6.7 suggest that the *k*-ω SST model is slightly better than the *k*-*ε* realizable model for the nine channel case.

The heat transfer coefficient determined for three different meshes are used to calculate the grid convergence index based on the methodology described in the Chapter V. Table 6.7 shows the GCI values calculated for the three meshes used to study the grid convergence. According to Table 6.7, the numerical uncertainty in the finest grid solution for the heat transfer coefficient is less than 1%. The GCI values reduce with grid refinement thereby suggesting grid convergence is obtained.

Table 6.6: Comparison of heat transfer coefficient using the SST k-ω model

Mesh Type	Mesh Size (No. of cells)	HTC-Numerical [W/m^2-K]	HTC-Experimental [W/m^2-K]
Coarse	746,000	11999	7184
Fine	895,000	11762.6	
Finest	1,119,000	11759.9	

Table 6.7: Comparison of the grid convergence index for the two turbulence models

Variable Name	Values for *k*-ε realizable turbulent model	Values for *k*- ω SST turbulent model
r_{21}	0.8335	0.8335
r_{32}	0.79982	0.79982
$\emptyset_1$	12917.1	11999
$\emptyset_2$	12622.0	11762.6
$\emptyset_3$	12623.6	11759.9
e_a^{21}	2.28%	1.97%
e_a^{32}	0.0126%	0.023%
e_{ext}^{21}	13.25%	13.6%
e_{ext}^{32}	0.0633%	0.127%
GCI_{21}	17.1%	14.7%
GCI_{32}	0.078%	0.144%

Figure 6.7 shows the heat transfer coefficient variation with dimensionless temperature T_b/T_{pc} for the three meshes using the *k*-ε realizable turbulent model. It can be observed that all the three meshes result in similar variation quantitatively and qualitatively. A similar plot is made with the *k*-ω SST turbulence model and is shown in Figure 6.8. All three meshes result in similar heat transfer coefficient values. It is also to be noted that as in the single case, the heat transfer coefficient peaks when the bulk temperature approaches the pseudocritical temperature, which is consistent with the theory. As evident from Tables 6.6 and 6.7, the *k*-ω turbulence model on finest mesh results in a better agreement with the experiments.

Figure 6.9 compares the heat transfer coefficeint calculated with the two different turbulence models using the finest meshes and the experiment values. The numerical value of the heat transfer coefficient is higher than the experimental value. However, the values differ by approximately 7% between the two turbulence models. This difference between the two turbulence models becomes significantly lower as the bulk temperature moves away from the critical temperature. Thus it is safe to conclude that these turbulence models are unable to capture the large variations in the properties of CO_2 in the pseudocritical region. A modification to these turbulence models is required to account for large property fluctuations in order to predict the heat transfer accurately using CFD methodology.

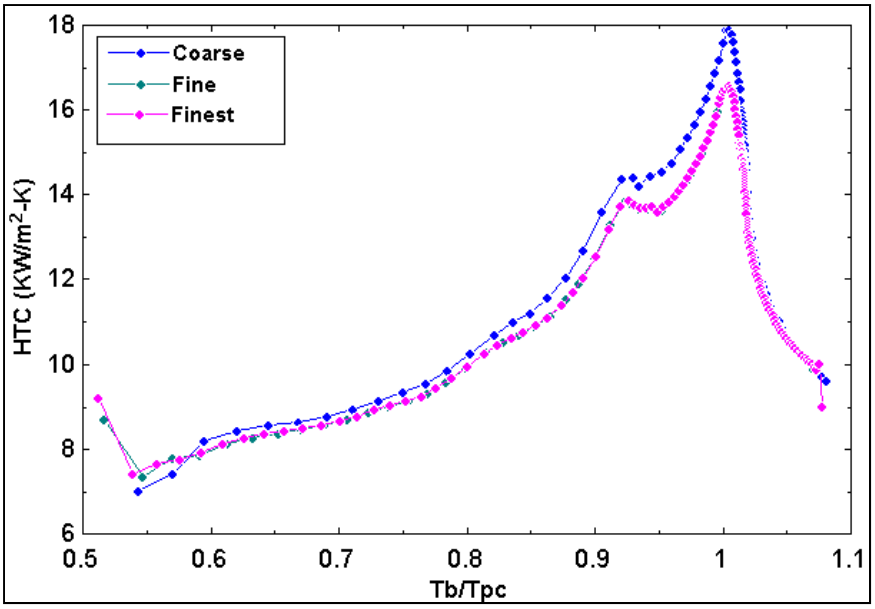

Figure 6.7: Comparison of heat transfer coefficient for different meshes using the k-ε realizable turbulence model

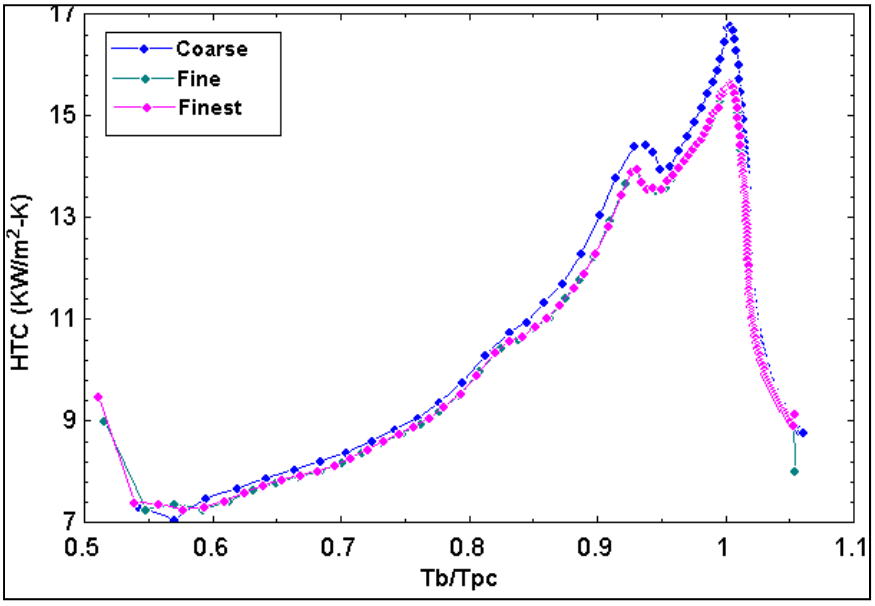

Figure 6.8: Comparison of heat transfer coefficient for different meshes using the k-ω SST turbulence model

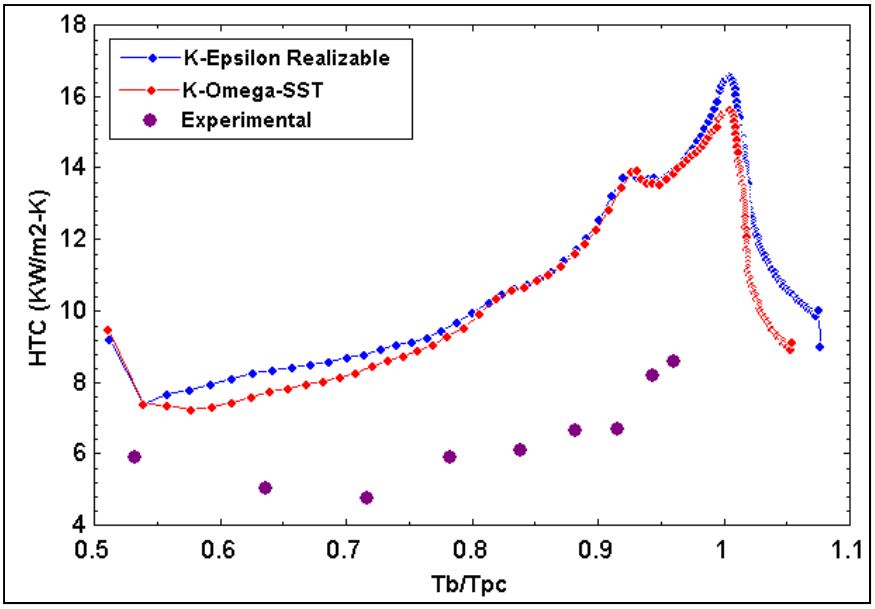

Figure 6.9: Comparison of numerical and experimental values of heat transfer coefficient on the finest mesh

Generally speaking, the thermo-physical properties vary drastically in the developing and boundary layer regions. Increasing heat flux has smaller effect on the distribution of the thermophysical properties than increasing Reynolds numbers. It is observed from Figure 6.10, that there is a drop in the density of the fluid at pseudocritical temperature. For the mass flux to remain constant an increase in the velocity is required. So the flow starts accelerating which increases the Reynolds number as shown in Figure 6.11. An increase in the Reynolds number makes the flow more turbulent (better mixing) therby increasing the heat transfer. There is also an increase in Prandtl number observed in Figure 6.12. Nusselt number, a parameter which helps in studying the heat transfer depends on both on the Reynolds as well as the Prandtl number. Thus an increase in these two numbers increases the Nusselt number, thus

increasing the heat transfer. These plots have similar trend as shown in the single channel case.

From the results obtained for a single channel and nine channels, the heat transfer coefficient is under predicted for single channel case while over predicted for nine channels when compared to the experiments. This could be because the mass flux differs in the single channel compared to an individual channel of the nine-channel geometry. There is a difference in the boundary layer in these geometries. The thickness of the boundary layer decreases with increase in mass flow rate. So the boundary layer in single channel is less thick compared to that individual channels in the nine-channel geometry. The flow is less turbulent because of less thickness of the boundary layer, decreasing the heat transfer in a single channel.

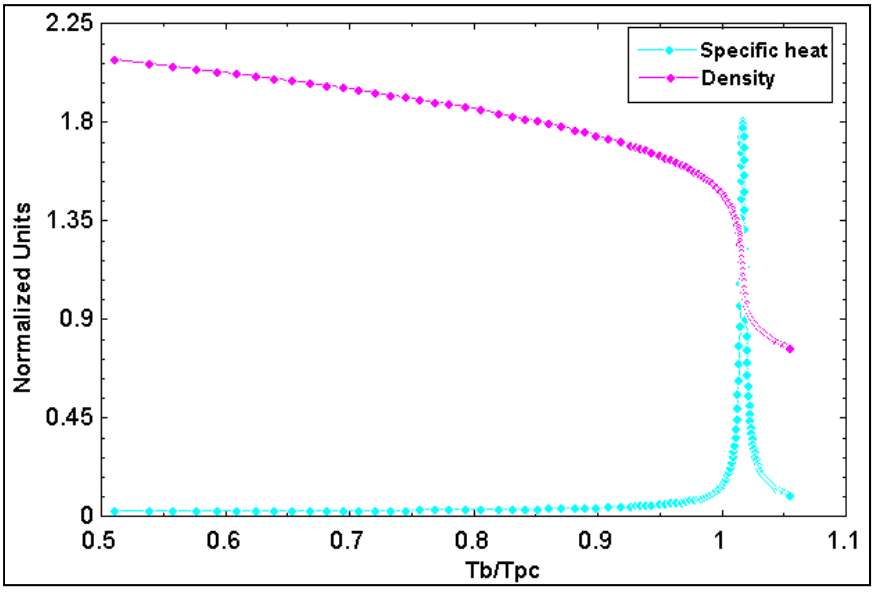

Figure 6.10: Variation of density and specific heat for nine channel case

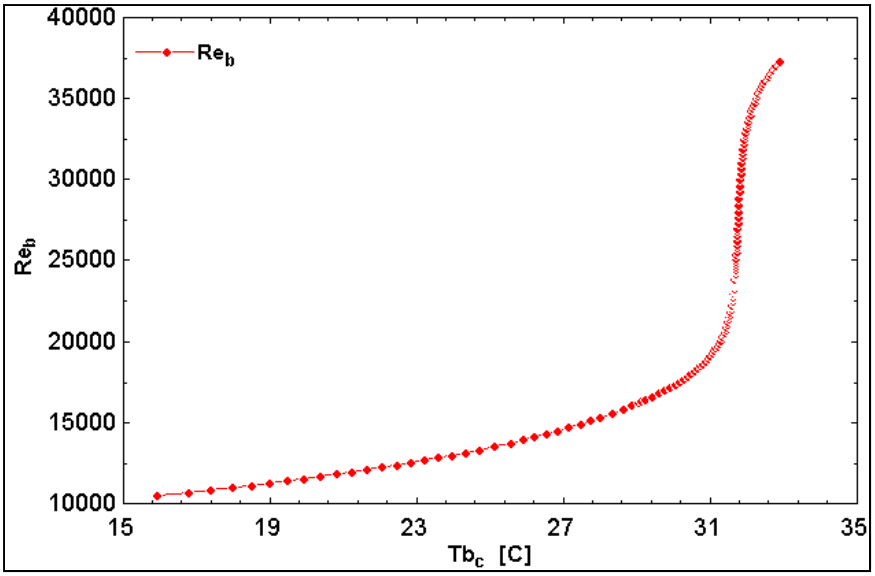

Figure 6.11: Variation of Reynolds number with bulk temperature for the nine channel case at M=761.94 kg/m^2-s, T_{in}=14.99^{o}C, P_{op}=7.5MPa

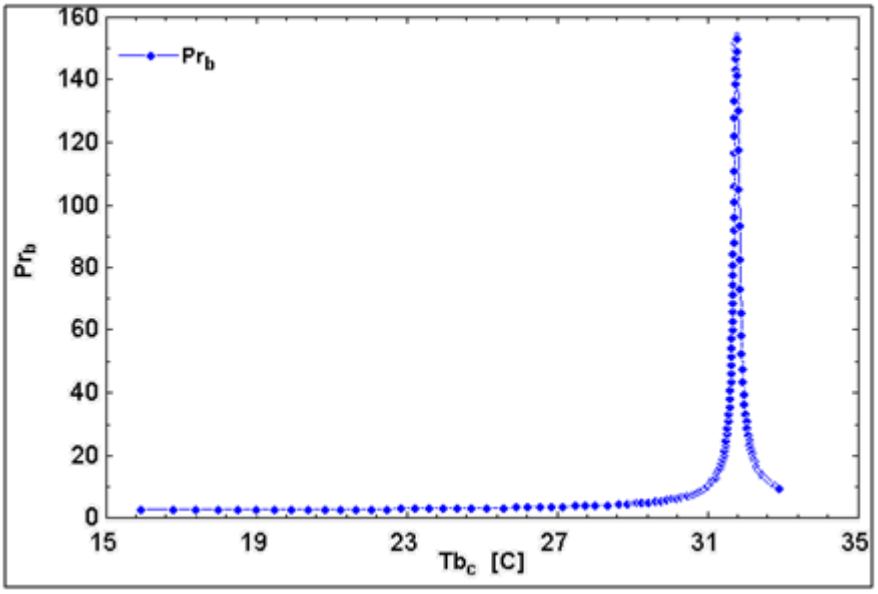

Figure 6.12: Variation of Prandtl number with bulk temperature for the nine channels case at M=761.94 kg/m^2-s, T_{in}=14.99^{o}C, P_{op}=7.5MPa

The local heat transfer was investigated in first (channel 1), last (channel 9) and center (channel 5) channel of the nine channel case. It is observed from Figure 6.13 that the heat transfer coefficient is slightly higher in the first and the last channels compared to the center channel.

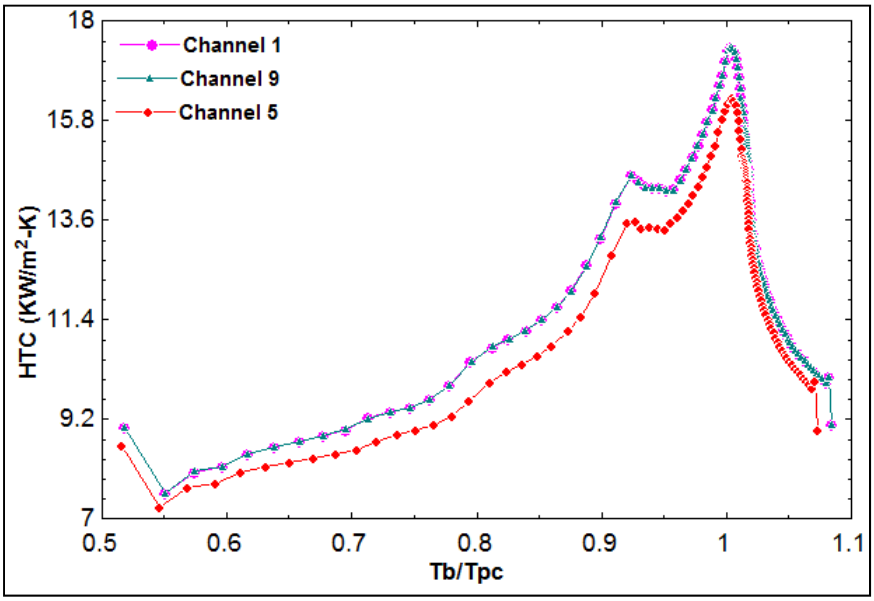

Figure 6.13: Comparison of heat transfer coefficient in the individual channels

6.2.1 Effect of mass flow rate on the heat transfer coefficient

The problem of nine channels is further investigated to study the heat transfer phenomenon by using a lower mass flux through the channels. A simulation was performed for inlet conditions of 14.99^{o}C and 7.5MPa operating pressure with a mass flux of 326 kg/m^2-s. The two turbulence models were compared for this lower mass flux.

It is observed from Figure 6.14 that the heat transfer coefficient was very similar for both the turbulence models. The the numerical simulation using the k-omega SST model was also compared to experiments. The results are shown in Figure 6.15. It is observed that the heat transfer calcualted numerically is higher than the experiments.

Figure 6.16 compares the heat transfer coefficient for two different mass fluxs, 762 and 326 kg/m^2-s with the same inlet temperature (14.99°C) and operating pressure (7.5MPa). From the plot it is observed that the heat transfer coefficient increases with an increase in the mass flux through the channels. This is because of the decrease in the Reynolds number for lower mass fluxes. Similar results would be observed for fluids at normal pressures.

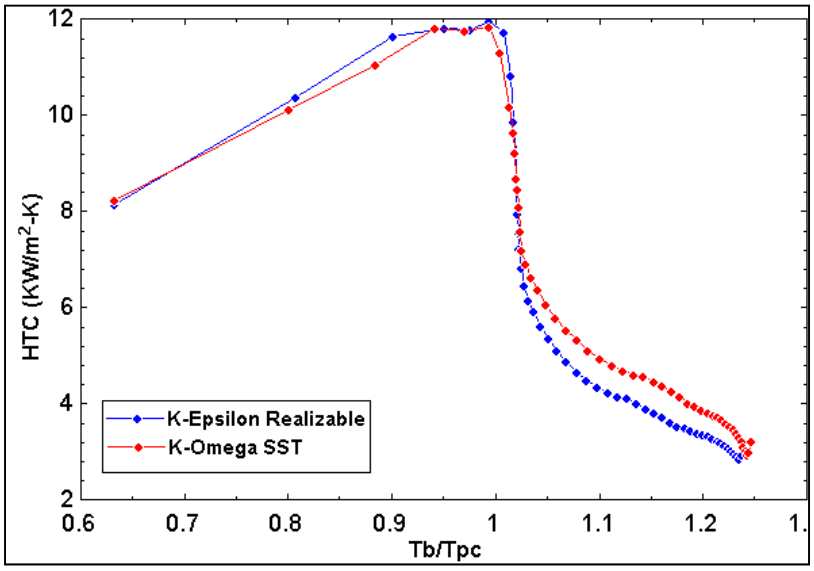

Figure 6.14: Comparison of heat transfer coefficient for two different turbulent models at a mass flux M = 326 kg/m^2-s

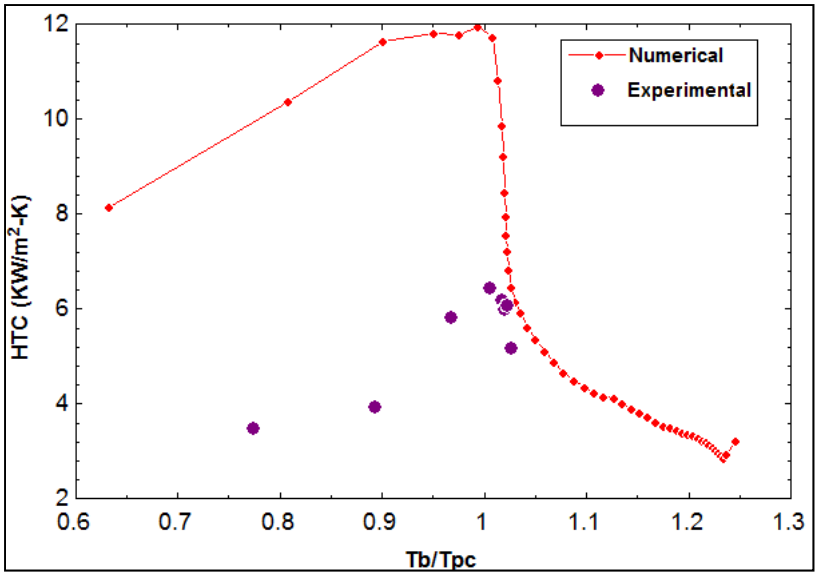

Figure 6.15: Comparison of heat transfer coefficient of k-ω and experiments at a mass flux of M = 326 kg/m^2-s

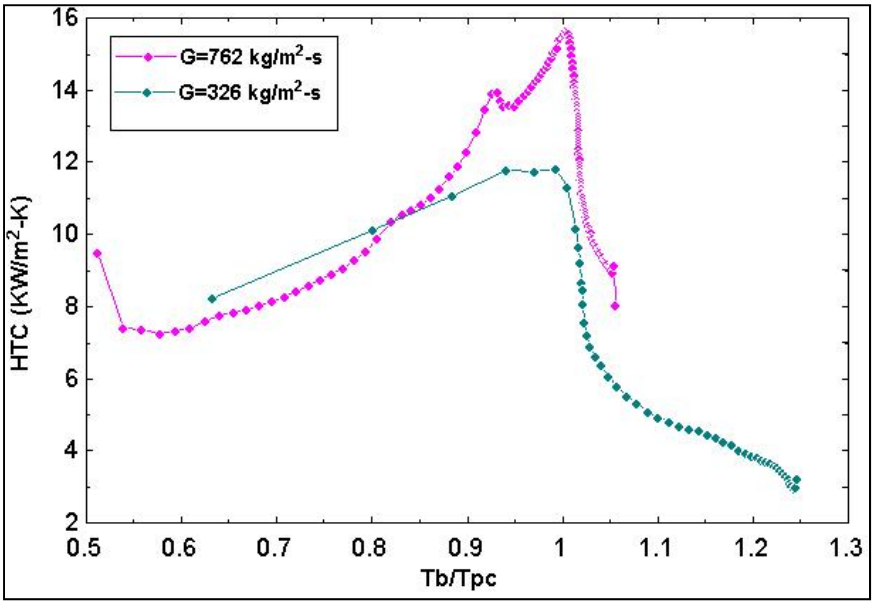

Figure 6.16: Comparison of heat transfer coefficient for two different mass fluxes

6.2.2 Effect of pressure on the heat transfer coefficient

Figure 6.17 shows the effect of increasing the operating pressure on the heat transfer coefficient.

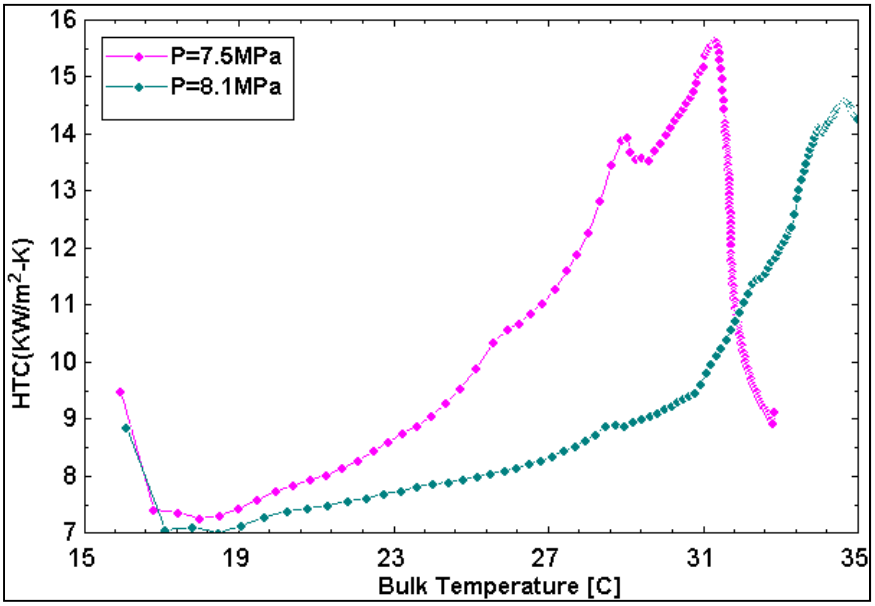

Figure 6.17: Comparison of heat transfer coefficient at operating pressures 7.5MPa and 8.1MPa

With an increase in pressure the temperature range of the pseudocritical region increases. In this study, the heat transefer coeffiecient is calculated at a pressures 7.5MPa and 8.1MPa pressures with the same inlet conditions. An inlet temperature of 14.99°C, a mass flux of 762 kg/m^2-s and same wall boundary conditions is used. It is observed that the peak in the heat transfer coefficient shifts to higher temperatures as the pressure is increased. This coincides with the shift in the pseudocritical temperatures as the pressure is increased.The variation of properties is maximum at the critical pressure

(7.5MPa in this case). The large fluctuations in properties reduce as the pressure moves away from the critical pressure, reducing the heat transfer enhancement of these fluids.

6.2.3 Comparison between the heat transfer in the cooling and heating mode

A simulation in carried out for the nine channel geometry with an inlet temperature of 60°C, an operating pressure of 7.5MPa and a mass flux of 762 kg/m^2-s in 'cooling mode' on the fine mesh using *k-ω* SST model. The temperature at the various axial locations along the top and bottom walls is shown in Table 6.8.The heat transfer obtained numerically in the cooling mode is compared to that of experiments in Figure 6.18. It is observed that the heat transfer predicted numerically is higher than that of experiments.

Table 6.8: Temperatures measured experimentally at the top and bottom wall

Axial (mm)	25	75	125	175	225	275	325	375	425	475
Tw_Top	37.9	35.4	33.63	32.57	31.42	30.23	30.62	30.23	29.96	29.5
Tw_Bottom	34.39	31.9	29.54	29.91	28.25	28.79	27.12	26.89	27.44	27.2

The results of the heat transfer coefficient obtained in the cooling mode are compared to that of the heating mode and is shown in Figure 6.19. It is observed that the Sc-CO_2 when cooled has higher heat transfer coefficient than that when heated. Olson *et al*., (2000) observed similar results of flow of carbon dioxide in a horizontal tube with a diameter of 10.9mm [25]. There has been less work done to study the heat transfer in

the cooling mode than the heating mode. Researchers should focus on designing more experiments in the cooling mode.

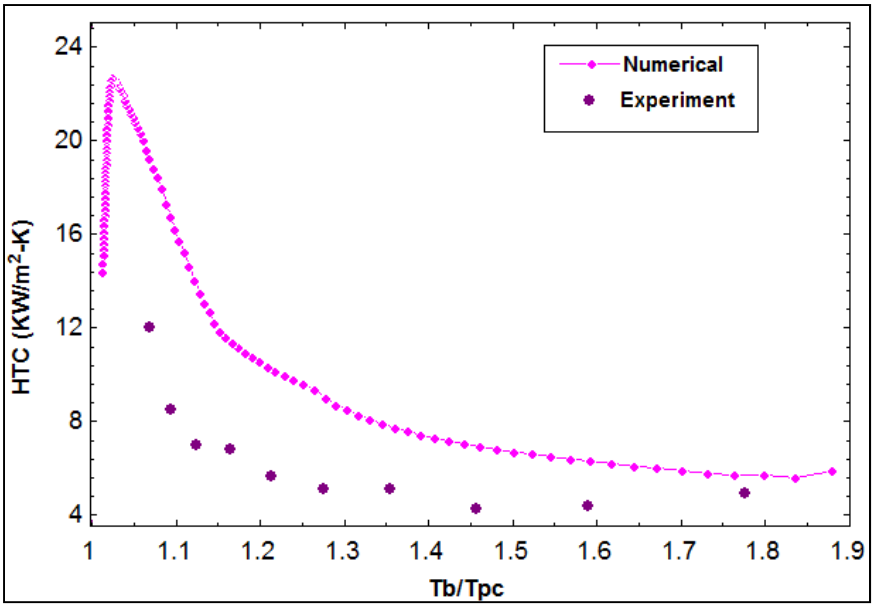

Figure 6.18: Comparison of heat transfer in the cooling mode to that of experiments

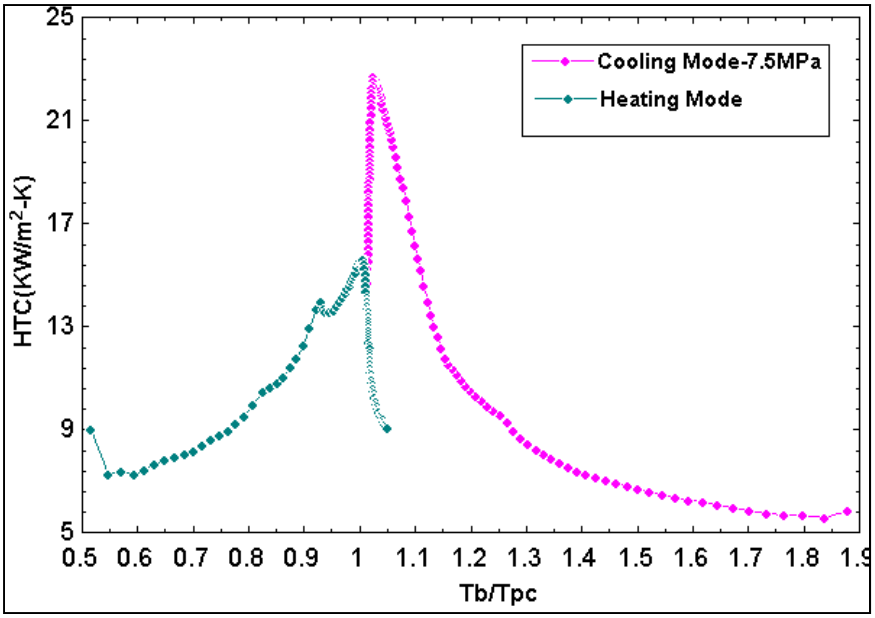

Figure 6.19: Comparison of heat transfer in the cooling and the heating mode

6.2.4 Comparison of heat transfer coefficient with correlations

There are several correlations existing the in literature for heat tranfer of Sc-CO_2. The average heat transfer coefficient was compared with the correlation developed by Dittus-Boetler [9], Jackson [17] and Liao [3] for the experiments in the heating mode. Figure 6.20 shows the numerical and experimental heat transfer with the some of the correlations existing in the literature.

Dittus Boelter proposed the heat transfer coefficient for forced convection in turbulent flows at Sc pressures. Since this correlation does not take in account the effect of variation in properties into consideration, the heat transfer coefficient was over predicted at the pseudocritical temperature compared to the CFD computations and experiments.

Both Jackson's and the Liao's correlations in heating mode underpredict the heat transfer coefficient at this temperature. Both these correlations take the effect of density fluctuations in the wall and bulk region as well as the specific heat and were developed for higher pressures (8.1MPa and 10.2MPa) where the bulk temperatures were far from T_{pc} . Also differences could also be attributed to the fact that these correlations were developed for circular tubes.

The numerical data was compared to the correlation developed by Alan in the nine and single channel cases [4]. Figure 6.21 shows the comparison of the heat transfer coefficient with this correlation. The heat transfer in a single channel is under predicted compared to the new correlation whereas it is over predicted in the nine channels.

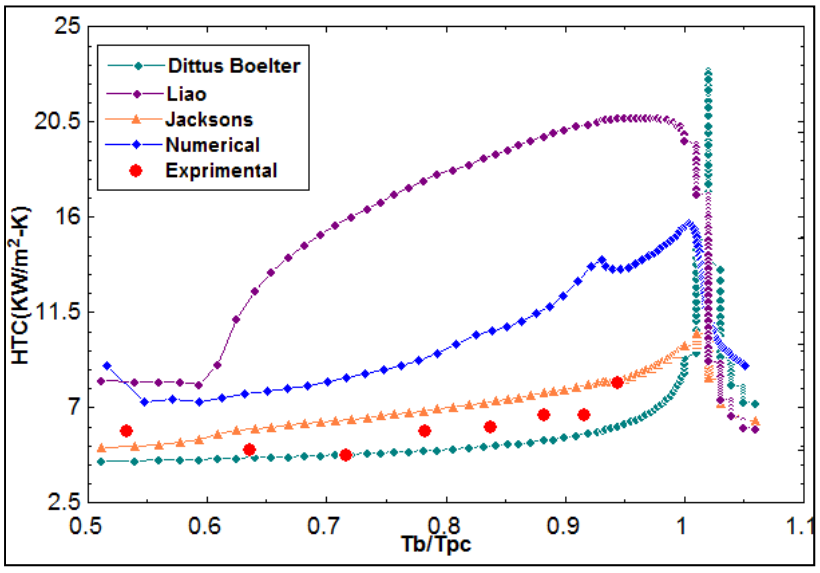

Figure 6.20: Comparison of heat transfer coefficient with Dittus Boelter's, Jackson's and Liao's correlations

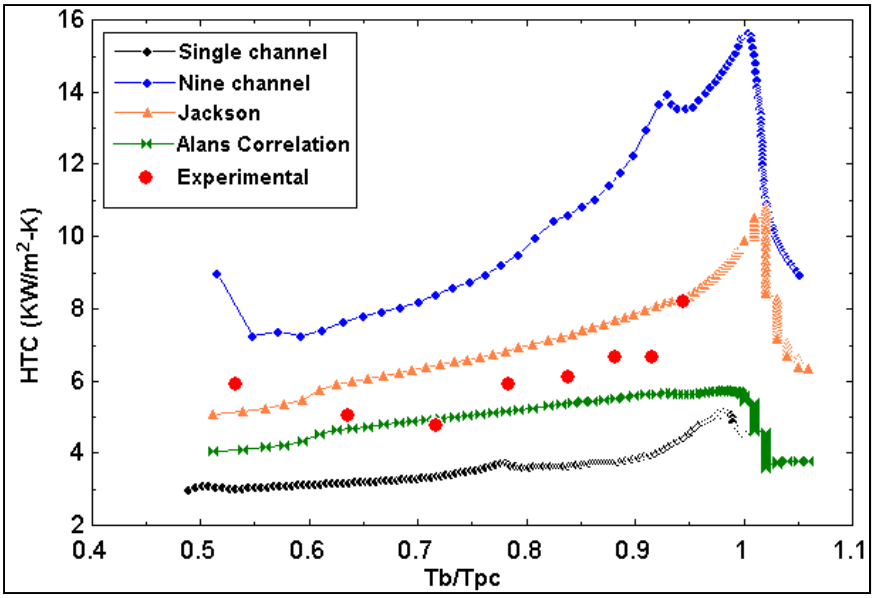

Figure 6.21: Comparison of numerical heat transfer coefficient with Jacksons and Alan's correlation for single and nine channel case

6.3 Zigzag channel geometry

Preliminary studies were carried out for zigzag channel geometry. A simulation at an inlet temperature of 14.99°C and a pressure of 7.5MPa with a mass flux of 761.94 kg/m^2-s in the heating mode is studied. The top and bottom wall temperatures of the test section are the same as tabulated in Table 6.1.

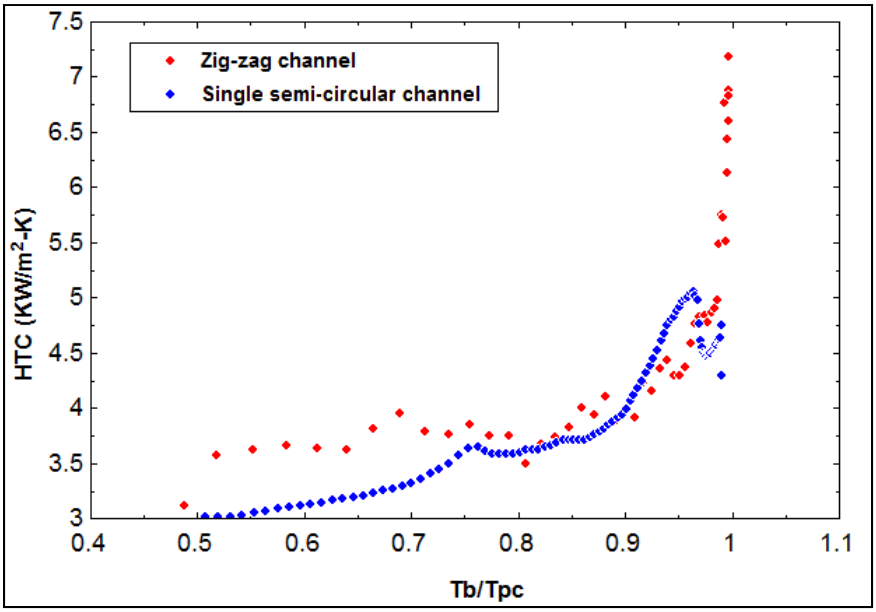

Figure 6.22: Variation of heat transfer coefficient for the zigzag channel case at M=761.94 kg/m2-s, Tin=14.99oC, Pop=7.5MPa

The results obtained for the heat transfer coefficient is shown in Figure 6.22. These results are compared to that of case 1. It is observed that the heat transfer coefficient is much higher compared to the semi-circular geometry. Also the comparison of bulk temperature with a semi-circular channel is shown in Figure 6.23. The bulk temperature is predicted higher than the semi-circular channel. The temperature contours are plotted and shown in Figure 6.24. From this plot it is observed that the temperature is higher at the bending sections than the interior.

The velocity vectors and the velocity contours in the zigzag channel geometry are shown in Figure 6.25 and 6.26. It is observed that the there are regions in the channel where the velocity increases and flow reversal (happens because of flow separation) occur. Figure 6.25 shows the change in the axial velocity along a segment of the zigzag

channel. The figure clearly shows the flow reversal occurring inside the zigzag channel. This plot further confirms that there are regions of reverse flow. Similar results were obtained by Dong *et al,* in his study of the zigzag channels [26].

It is known that the heat transfer from the fluid in the region of flow reversal decreases. On the other hand the heat transfer coefficient increases due to flow acceleration at the channel bending points. The net heat transfer as shown in Figure 6.22. As can be seen the heat transfer coefficient is higher in the zigzag channel compared to a single semicircular channel. This is because of the higher surface area of the zigzag channel as compared to a semicircular channel and a continuously accelerating flow.

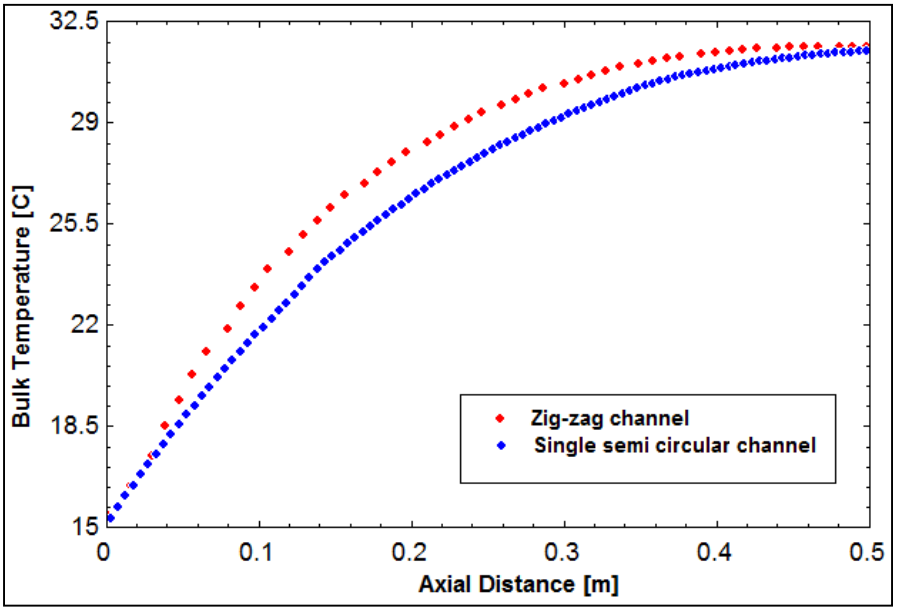

Figure 6.23: Axial variation of bulk temperature for the zigzag channel case at M=761.94 kg/m^2-s, T_{in}=14.99^{o}C, P_{op}=7.5MPa

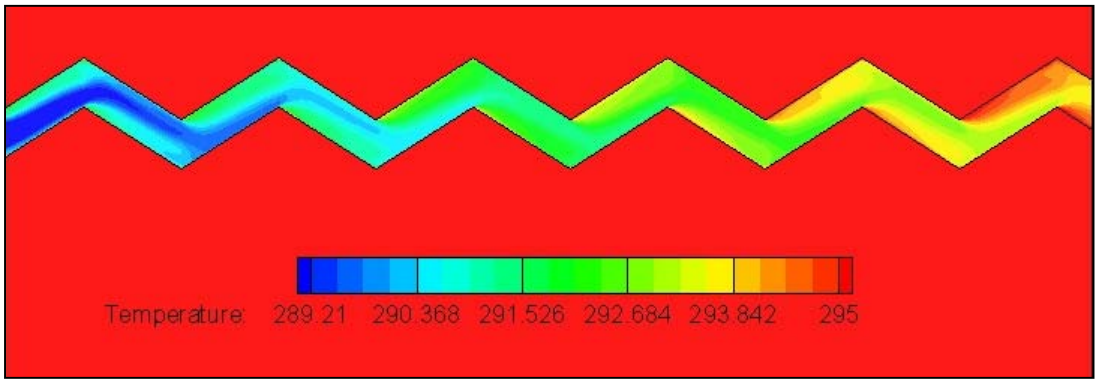

Figure 6.24: Temperature contours at for a segment of the zigzag channel case at M=761.94 kg/m^2-s, Tin=14.99^{o}C, P_{op}=7.5MPa

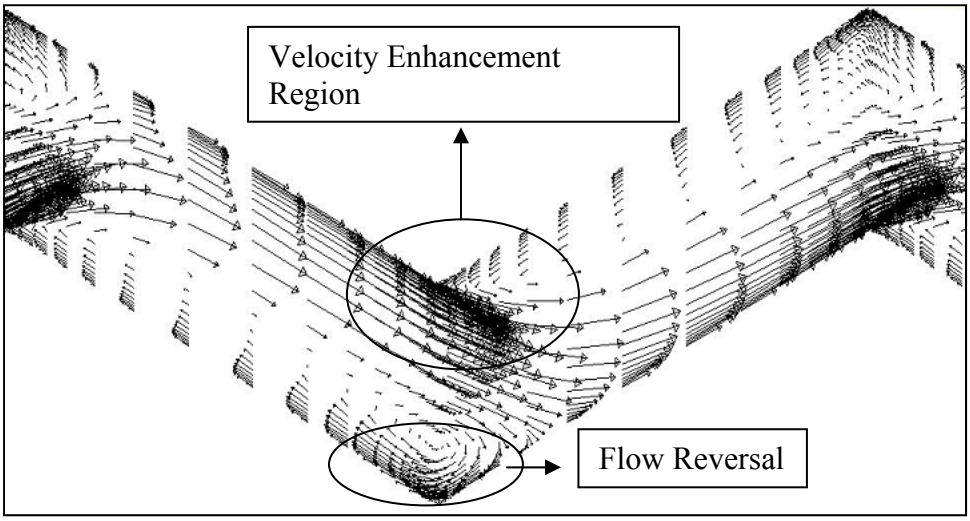

Figure 6.25: Velocity vectors in a segment of the zigzag channel at M=761.94 kg/m^2-s, T_{in}=14.99^{o}C, P_{op}=7.5MPa

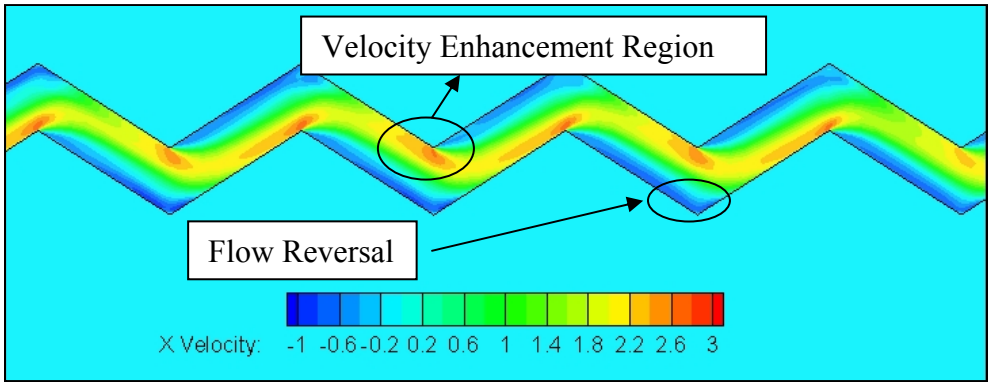

Figure 6.26: Velocity contours at M=761.94 kg/m^2-s, T_{in}=14.99^{o}C, P_{op}=7.5MPa

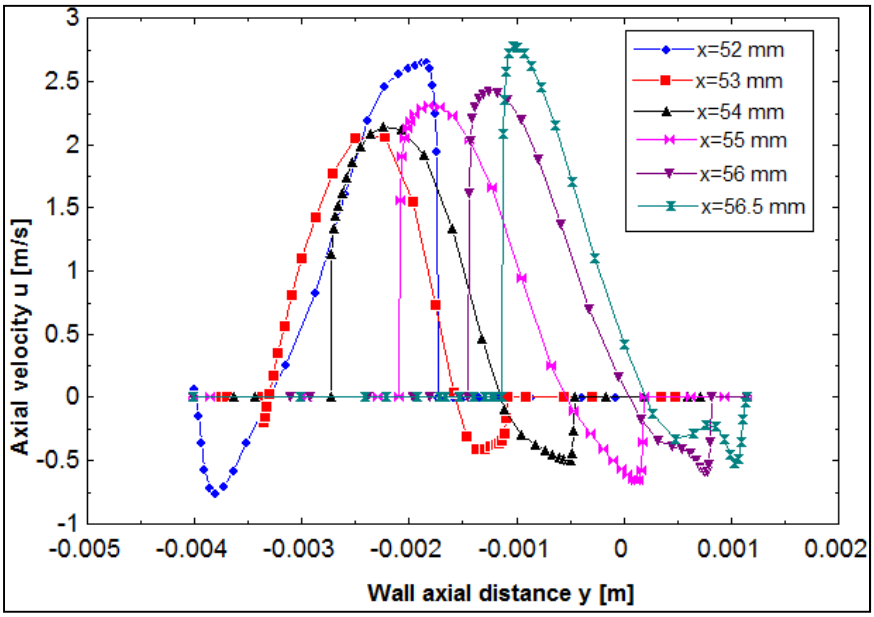

Figure 6.27: Velocity profiles in a segment of the zigzag channel

6.4 Pressure drop

The pressure drop in case 1 is compared to that of first channel of the case 2. This comparison is shown in Figure 6.28. The chart is plotted with dimensionless pressure which is defined as $\frac{p}{\left(\frac{1}{2}\rho_\infty u^2{}_\infty\right)}$, where ρ_∞ is the inlet density and u_∞ is the inlet velocity. It is observed that the non-dimensional pressure is higher in case 2 compared to case 1. This is because the velocity is higher in case 1 than case 2. However actually pressure drop is 4.5 kPa in the case 1 and 1.6 kPa in the center channel of the case 2.

This non-dimensional pressure is evaluated for a segment (from x=52mm to x=61mm) of the zigzag channel as shown in Figure 6.29. It is observed that the in one segment of the zigzag channel the pressure decreases by a magnitude of 6. There are 110 such zigzag segments in the entire geometry, so a huge pressure drop occurs in the entire channel. This pressure drop is higher than that of case 1 and case 2.

A contour plot of the pressure varying along the zigzag channel is shown in Figure 6.30. It is observed that there is a high pressure at the bending points. This is attributed to the flow separation. The region of flow separation offers more resistance to the flow creating a high pressure drop. Therefore several bending sections in the entire zigzag channel highly increase the overall pressure.

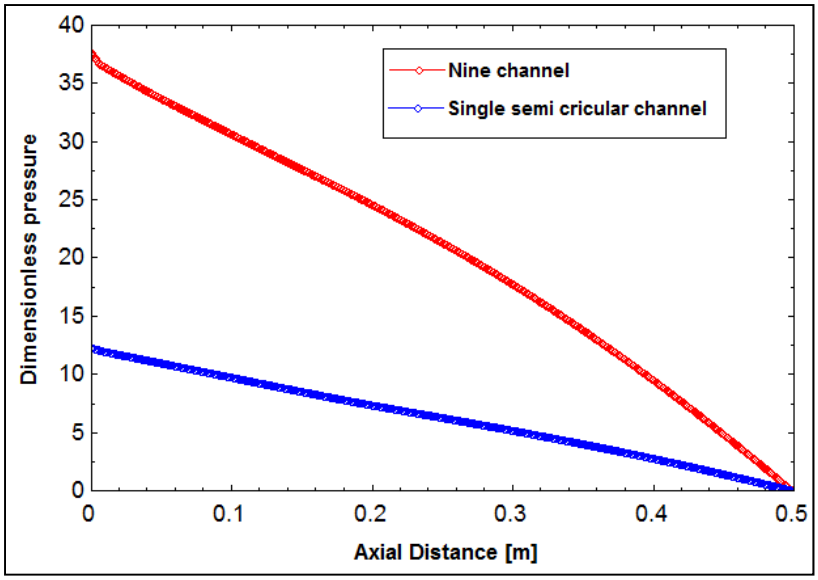

Figure 6.28: Axial variation of dimensionless pressure for cases 1 and 2 at M=761.94 kg/m^2-s, T_{in}=14.99^{o}C, P_{op}=7.5MPa

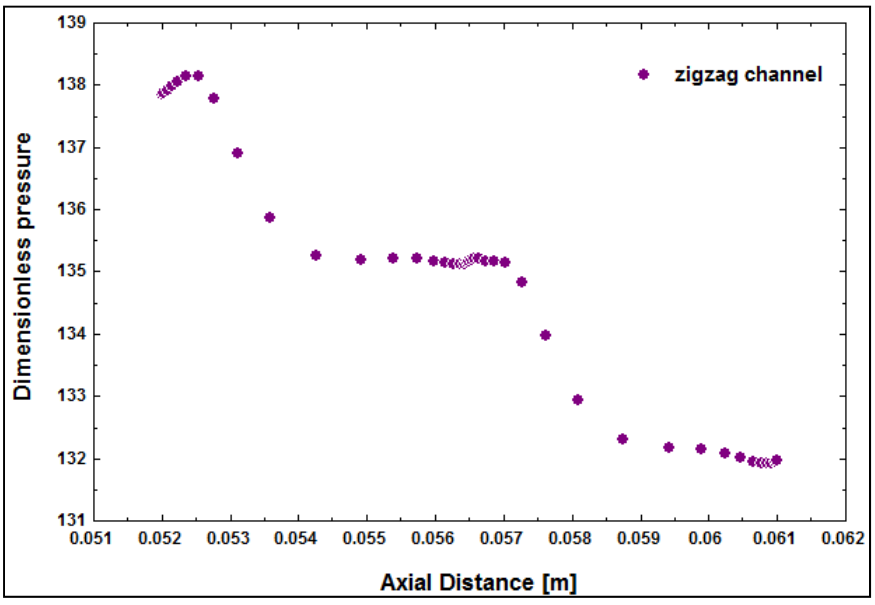

Figure 6.29: Axial variation of dimensionless pressure from x=52 to x=61 mm at M=761.94 kg/m^2-s, T_{in}=14.99^{o}C, P_{op}=7.5MPa

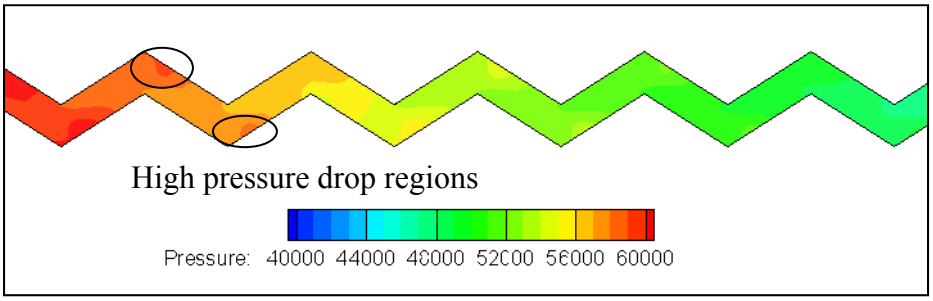

Figure 6.30: Contour plot of axial variation of pressure drop for zigzag channel at M=761.94 kg/m^2-s, Tin=14.99^{o}C, P_{op}=7.5MPa

CHAPTER VII

CONCLUSION

The problem of forced convection heat transfer of Sc-CO_2 in a series of mini semi-circular horizontal tubes and a zigzag shaped horizontal channel was investigated numerically using commercial code FLUENT (version 12.0) Three dimensional Computational Fluid Dynamics (CFD) models were developed to simulate the flow and heat transfer for three different geometries – a single semi-circular channel, a series of nine parallel semi-circular channels having an inside diameter of 1.9 mm and a zigzag channel. Several flow conditions were simulated to have a better understanding of heat transfer in these fluids in these geometries. Grid and accuracy refinement studies were carried out on these geometries to assess numerical errors. The k-ε realizable and the k-ω SST turbulence models were compared. All the computational meshes developed for this study incorporated the first node cell within the viscous sub-layer i.e. $y^+<1$.

The following observations were made from the single channel study:

1) The k-ε realizable model with enhanced wall treatment performed better than the k-ω SST turbulence models for single channel case. There was a difference of 1000 in the heat transfer coefficient values for these two models.
2) Enhancement in heat transfer coefficient at the pseudocritical point is observed. The reason in the enhancement is attributed to the increase in the specific heat and density of these fluids at pseudocritcal point.

3) A peak in the Reynolds and Prandtl numbers was observed in the numerical simulation. The peak in Reynolds number is attributed to drop in the density and that of Prandtl number is due to peak in the specific heat.
4) The heat transfer in the single channel was compared to the experiments. It is observed that heat transfer was under predicted when compared to the experiments. This could be because heat transfer in single channel differs from that in the test section which consists of nine channels.

The problem was further investigated for a nine channel case. The following conclusions could be drawn from the nine channel study:

1) The k-ω SST turbulence model predicted better results for the nine channel case. The heat transfer coefficient obtained numerically was over predicted compared to that of experiments. From the two cases studies it can be concluded that the two turbulence models are unable to capture the large variations in the properties of CO_2 in the pseudocritical region. A modification to these turbulence models is required to account for large property fluctuations in order to predict the heat transfer accurately using CFD methodology.
2) The two turbulence models were compared for this lower mass flux. It is observed that the heat transfer coefficient was very similar for both the turbulence models. The heat transfer coefficient increases with an increase in the mass flux through the channels.
3) The effect of increasing the operating pressure on the heat transfer coefficient was also studied numerically. It was observed that with an increase in pressure

the temperature range of the pseudocritical region increases. It is observed that the peak in the heat transfer coeffiecient shifts to higher temperatures as the pressure is increased. This coincides with the shift in the pseudocritical temperatures as the pressure is increased.

4) The experiments in the heating and cooling mode were also compared. It is observed that the Sc-fluids when cooled have higher heat transfer coefficient than that when heated. There is very less data existing in the literature for experiments in the cooling mode. More work needs to be done to study the heat transfer in cooling mode.
5) The heat transfer coefficient was compared to some of the correlations existing in the literature. It is observed that the Dittus Boelter correlation over predict the results compared to numerical and experimental data. This is because this correlation does not take into account the large variations in thermophysical properties. Further the heat transfer coefficient was compared to the Jackson's and Liao's correlations which take the property variations into account. But these correlations were developed for higher pressures, so at 7.5MPa pressures the results obtained numerically did not match very well. Further the numerical heat transfer was compared to correlation developed by Alan, it was observed that the numerical results for nine channels were over predicted and that of single channel were under predicted.

The problem was also investigated in single zigzag geometry. The following observations could be made:

1) The heat transfer predicted in this geometry was much higher than that predicted in case 1. This could be attributed to the shape of the geometry.
2) There is velocity enhancement as well as the flow reversal regions. The velocity enhancement regions increase the heat transfer as the flow becomes more turbulent. But the flow reversal regions reduce it because of flow separation. But average heat transfer is higher in this geometry.

The pressure drop across all these geometries was also studied.

1) The pressure drop was found to be higher in the zigzag geometry compared to the semicircular channels. This is expected result. The separated flow near the bending point in each segment of the zigzag channel causes resistance to the flow. Several such bending points in the entire geometry increase the total pressure drop significantly.

CHAPTER IX

FUTURE WORK

The possible future work for studying the thermal hydraulic behavior of Sc-CO_2 is summarized below:

- A further investigation on turbulent models is required which will be accurately capture the physics of the problems arising essentially due to significant variations in thermophysical properties in the critical and pseudocritical regions. The development of such effective turbulent models will be a breakthrough in this research area.
- Further investigation is required for the zigzag channel case. Grid refinement studies can be carried out for the zigzag channels.
- Affect of orientation of the test section (vertical vs. horizontal) is another problem that could be investigated in these channels.

REFERENCES

[1] V. Dostal, A supercritical carbon dioxide cycle for next generation nuclear reactors, Doctoral thesis, Department of Nuclear Engineering, MIT, Boston, 2004.

[2] I.L. Pioro, F.Hussam Khartabil, B. Romney Duffy, Heat transfer to supercritical fluids flowing in channels-empirical correlations(survey), *Nuclear Engineering and Design 230 (2004) 69-91.*

[3] S.M. Liao, T.S. Zhao, Measurements of heat transfer coefficients from supercritical carbon dioxide flowing in horizontal mini/micro channels, *Journal of Heat Transfer, 24, (June 2002)413-420.*

[4] A. Kurizenga, Heat transfer and pressure drop measurements in prototypic heat exchangers for the supercritical carbon dioxide Brayton power cycles, Doctoral thesis, University of Wisconsin, Madison 2010.

[5] K. Nikitin, Y. Kato, L. Ngo, Printed circuit heat exchanger thermal-hydraulic performance in supercritical CO2 experimental loop, *International Journal Refrigeration, 29, (2006) 807-14.*

[6] ANSYS® Academic Research, Release 12.0. help system, FLUENT Guide, ANSYS, Inc., Northbrook, IL, 2009.

[7] E. Schmidt, E. Eckert, V. Grigull, Heat transfer by liquids near the critical state, AFF Translation, No 527, Air Materials Command, Wrigth Field Dayton, OH, 1946.

[8] I. Pioro, R. Duffey, Experimental heat transfer to water flowing in channels at supercritical pressures (survey), in: Proceedings of the ANS/ENS International

Winter Meeting and Nuclear Technology Expo, Embedded Topical Meeting GLOBAL 2003 Advanced Nuclear Energy and Fuel CycleSystems, New Orleans, Louisiana, November 16–20, 2003.

[9] F.W. Dittus, L.M.K. Boelter, Heat transfer in automobile radiators of the tubular type, *University of California Publications in English, Berkeley, 2, (1930) 443–461.*

[10] M.E. Shitsman, Impairment of the heat transmission at supercritical pressures, *High Temperatures (ctp. 267–275) 1, 2 (1963) 237–244.*

[11] H.S. Swenson, J.R. Carver, C.R. Karakala, Heat transfer to supercritical water in smooth-bore tubes, *Journal of Heat Transfer, Trans. ASME, Ser. C 87 (4),(1965) 477–484.*

[12] E.A. Krasnoshchekov, V.S. Protopopov, About heat transfer in flow of carbon dioxide and water at supercritical region of state parameters, (in Russian), *Thermal Engineering. 10, (1960) 94.*

[13] E.A. Krasnoshchekov, V.S. Protopopov, I.A. Parkhovnik, V.A. Silin, Some results of an experimental investigation of heat transfer to carbon dioxide at supercritical pressure and temperature heads of up to 850 °C, *High Temperatures ctp. 1081–1084, 9 (5), (1971) 992–995.*

[14] K. Yamagata, K. Nishikawa, S. Hasegawa, Forced convective heat transfer to supercritical water flowing in tubes, *Int. Journal. Heat Mass Transfer 15 (12), (1972) 2575–2593.*

[15] A.A. Bishop, R.O. Sandberg, L.S. Tong, Forced convection heat transfer to water at near-critical temperatures and supercritical pressures, in: Report WCAP-2056, Part IV, November, Westinghouse Electric Corp., Pittsburgh,(1964).

[16] J.D. Jackson, J. Fewster, Forced convection data for supercritical pressure fluids, *HTFS (1975) 21540.*

[17] J.D. Jackson, Consideration of the heat transfer properties of supercritical pressure water in connection with the cooling of advanced nuclear reactors, in: Proceedings of the 13th Pacific Basin Nuclear Conference, Shenzhen City, China, October 21–25*,* (2002).

[18] J. Pettersen, R. Rieberer, S.T. Munkejord, Heat transfer and pressure drop for flow of supercritical and subcritical CO_2 in microchannel tubes, in: Final Technical Report, SINTEF Energy Research, Trondheim, Norway, (2000).

[19] X.L. Huai, S. Koyama,T.S. Zhao, An experimental study of flow and heat transfer of supercritical carbon dioxide in multi-port channels under cooling conditions, *Chemical Engineering Science, 60, (2005), 3337-3345.*

[20] J.Licht, M.Anderson, M.Corradini, Heat transfer to water at supercritical pressures in circular and square annular flow geometry, *International Journal of Heat and Fluid Flow, 29, (2008), 156166.*

[21] Thermophysical Properties of Fluid Systems [DB/OL] [2009-3 21], National Institute of Standards and Technology, http://webbook.nist.gov/chemistry/fluid.

[22] T. J. Barth, D. Jespersen, The design and application of upwind schemes on unstructured meshes, in: Technical Report AIAA-89-0366, AIAA 27th Aerospace Sciences Meeting, Reno, Nevada, (1989).

[23] R. D. Rauch, J. T. Batira, N. T. Y. Yang, Spatial Adaption Procedures on unstructured meshes for accurate unsteady aerodynamic flow computations, in: Technical Report AIAA-91-1106, American institute of aeronautics and astronauts, California,*(1991).*

[24] C. Freitas, Journal of fluids engineering editorial policy statement on the control of numerical accuracy, *ASME Journal of Fluids Engineering., 115, (1993) 339–340.*

[25] D.A. Olson, Heat transfer of supercritical carbon dioxide flowing in a cooled horizontal tube, in: Proceedings of 4th IIR-Gustav Lorentzen Conference on Natural Working Fluids, Purdue University, *(2000) 251–258.*

[26] D.E. Kim, M.H. Kim, J.E. Cha, S.O. Kim, Numerical investigation on thermal–hydraulic performance of new printed circuit heat exchanger model, *Nuclear Engineering Des. 238,(2008) 3269–3276*.

APPENDIX A

MANIFOLD STUDY

Manifold Study

To understand the inlet and the exit effects, there was a need to study the flow of carbon dioxide into the manifold. In the actual experiment the flow the channels is through an inlet manifold. A mesh was generated using Gambit, it consists of 67,000 cells. The simulations are carried on Fluent.

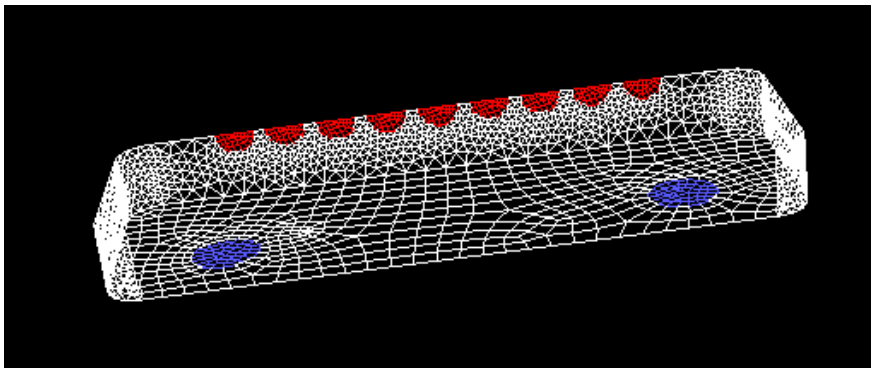

Figure A.1: Meshed geometry of the Manifold

The Figure A.2 shows the velocity vetors for inlet temperature of 14.99 C and a mass flux of 761.94 kg/m^2-s. The velocity vectors at the inlets are uniform. There are no stangnation points or re-circulation zones observed. The velocity adjacent to the walls is zero because of the no-slip condition. The velcity at the inlets is evaluated from the

mass flux specified at the inlets. The velocity of the fully developed flow inside these inlets is 0.598m/s.

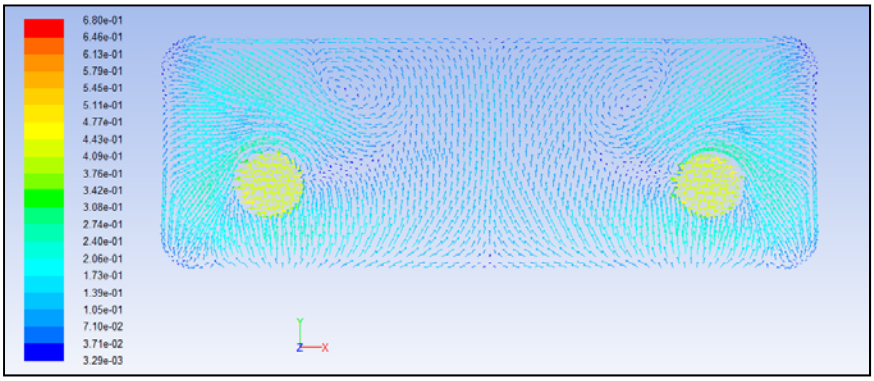

Figure A.2: Velocity contours for the above case

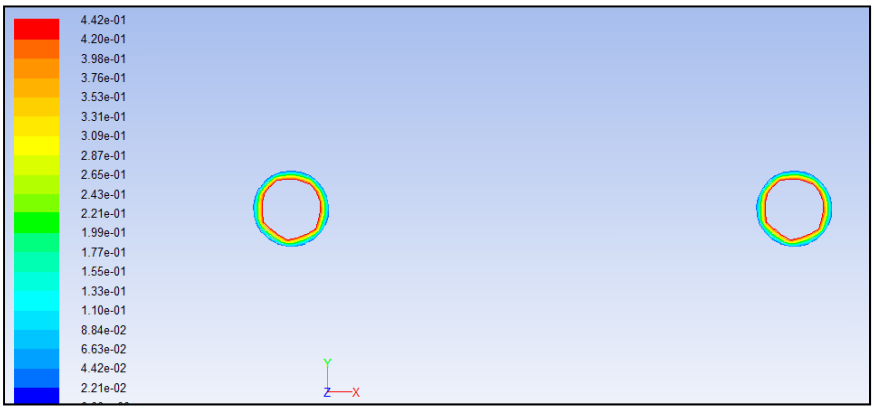

Figure A.3: Velocity contour of the inlets

Vector plot for the outlets is shown in Figure A.4. It is observed from this plot that the outlet has uniform flow.

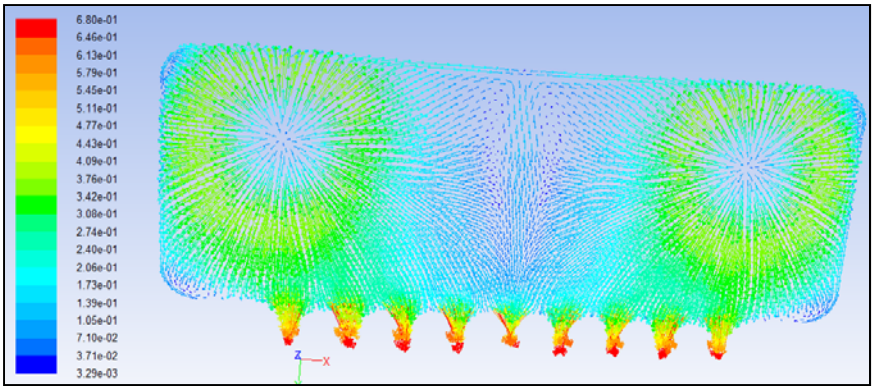

Figure A.4: Velocity vector plot

Temperature contours in the first, last and the center channels at the outlet is shown in Figure A.5. The maximum velocity is 0.671m/s. These plots give an idea of the velocity profile in the respective semi-circular channels. It is observed that the velocity in the first channel is smoother that is the gradient is less compared to the center and the last channel. Velocity is almost constant in each of the channels but the flow pattern differs in each of the channel. So focus on studying the local flow properties in each of these channels is required. The contour plots both away from the critical point at the critical point have similar profiles. The velocity increases in the pseudo-critical region but the profiles are similar.

The mass flow rate in each of the nine channels was evaluated for above mentioned inlet temperature. It is observed from Figure A.6 that the mass flow rate is more in the first and the last channels compared to the remaining channels. The standard deviation (of the order 10^{-5}) is very small so we can consider the flow to be almost constant.

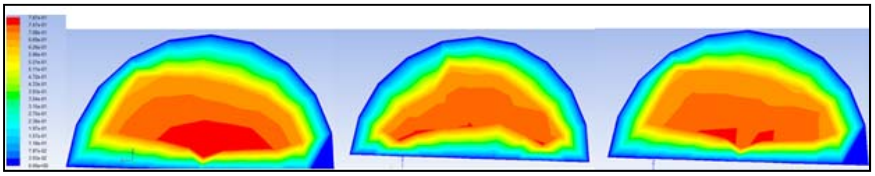

Figure A.5: Temperature contours of the first, last and middle channel

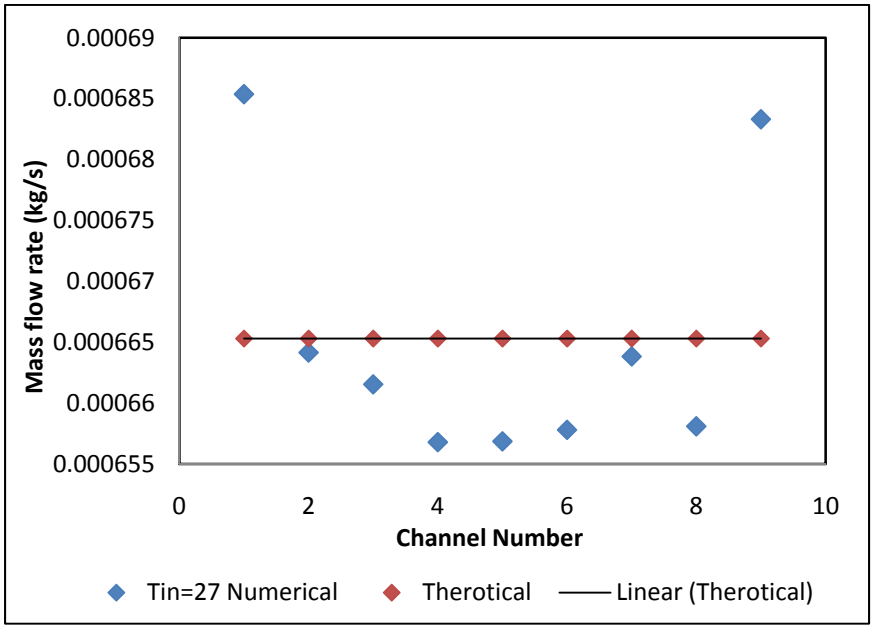

Figure A.6: Comparison of mass flow rate in each of nine channels

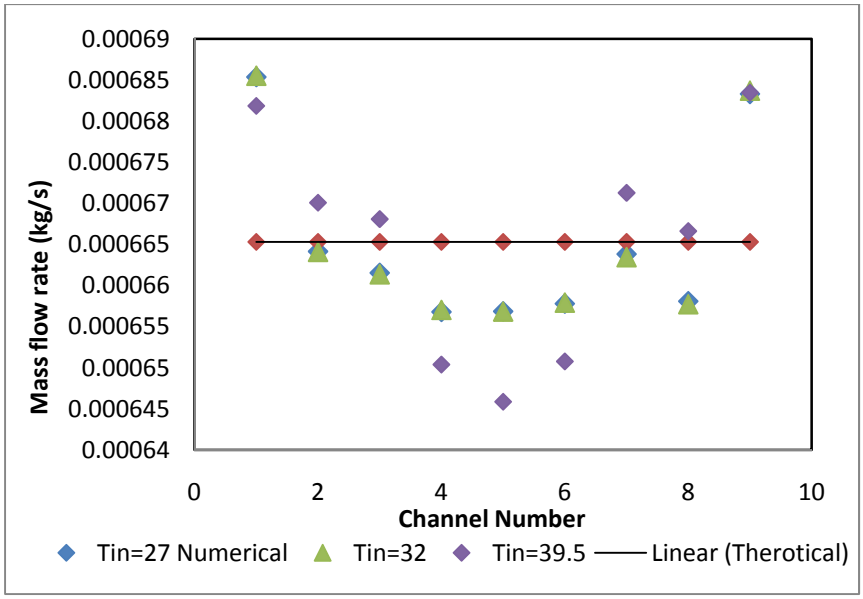

Figure A.7: Comparison of the mass flow in each channel with varying inlet temperature

Figure A.7 compares the results of mass flow rate at varying inlet temperatures (27, 32 and 39.5°C) and at a pressure of 7.5MPa. It is observed in the flow rates at 27 and 32°C are almost the same, compared to that at 39.5°C. Similar trend is observed for all the three cases. Thus it can be concluded that assuming the same mass flux in each channel is a reasonable assumption.

VITA

Name: Roma Fatima

Place of Birth: Hyderabad, India

Permanent Address: Department of Mechanical Engineering, Birla Institute of Technology and Sciences, Pilani-333031

Education **Texas A&M University, College Station, Texas**

Master of Science in Mechanical Engineering, December 2010.

Birla Institute of Technology and Sciences (BITS), Pilani, Rajasthan, India

Master of Science in Physics, Graduated in May 2008.

Bachelor of Engineering in Mechanical, Graduated in May 2008.

Academic Experience

Research Scholar under Dr Mark Anderson at University of Wisconsin - Madison, May 2010-August 2010.

Research Assistant at Texas A&M University

Numerical Study of Thermal Hydraulic Behavior of Super-critical Fluids

Teaching Assistant at Texas A&M University, August 2008-August 2009**,** Courses tutored included Principles of Thermodynamics, Thermo Fluid Analysis and Engineering Analysis.